



HAL
open science

Thermal tides on Mars before and during the 2018 Global Dust Event as observed by TIRVIM-ACS onboard ExoMars Trace Gas Orbiter

Sandrine Guerlet, S Fan, François Forget, N Ignatiev, Ehouarn Millour, A Kleinböhl, A Shakun, A Grigoriev, A Trokhimovskiy, Franck Montmessin, et al.

► To cite this version:

Sandrine Guerlet, S Fan, François Forget, N Ignatiev, Ehouarn Millour, et al.. Thermal tides on Mars before and during the 2018 Global Dust Event as observed by TIRVIM-ACS onboard ExoMars Trace Gas Orbiter. *Journal of Geophysical Research. Planets*, In press, 10.1029/2023JE007851 . insu-04183247v1

HAL Id: insu-04183247

<https://insu.hal.science/insu-04183247v1>

Submitted on 18 Aug 2023 (v1), last revised 15 Sep 2023 (v2)

HAL is a multi-disciplinary open access archive for the deposit and dissemination of scientific research documents, whether they are published or not. The documents may come from teaching and research institutions in France or abroad, or from public or private research centers.

L'archive ouverte pluridisciplinaire **HAL**, est destinée au dépôt et à la diffusion de documents scientifiques de niveau recherche, publiés ou non, émanant des établissements d'enseignement et de recherche français ou étrangers, des laboratoires publics ou privés.



Distributed under a Creative Commons Attribution - NonCommercial 4.0 International License

Thermal tides on Mars before and during the 2018 Global Dust Event as observed by TIRVIM-ACS onboard ExoMars Trace Gas Orbiter

S. Guerlet^{1,2*}, S. Fan¹, F. Forget¹, N. Ignatiev³, E. Millour¹, A. Kleinböhl⁴, A. Shakun³, A. Grigoriev⁵, A. Trokhimovskiy³, F. Montmessin⁶ and O. Korablev³

¹LMD/IPSL, Sorbonne Université, PSL Research University, École Normale Supérieure, École

Polytechnique, CNRS, Paris, France

²LESIA, Observatoire de Paris, CNRS, Sorbonne Université, Université Paris-Diderot, Meudon, France

³Space Research Institute (IKI), Moscow, Russia

⁴Jet Propulsion Laboratory, California Institute of Technology, Pasadena, CA, USA

⁵Research School of Astronomy and Astrophysics, Australian National University, Canberra, ACT 2611,

Australia

⁶LATMOS/IPSL, Guyancourt, France

Key Points:

- The characteristics of the migrating tides derived from TIRVIM at $L_s=150^\circ$ agree with tidal theory and model predictions.
- During the 2018 Global Dust Event, the diurnal tide reached an amplitude of 35K at 65°S and we tentatively detect the ter-diurnal tide.
- During the 2018 GDE, the semi-diurnal tide amplitude reached 10K at 20°S and exhibited a phase tilt with latitude.

*4 Place Jussieu, Paris, France

Corresponding author: Sandrine Guerlet, sandrine.guerlet@lmd.jussieu.fr

This article has been accepted for publication and undergone full peer review but has not been through the copyediting, typesetting, pagination and proofreading process, which may lead to differences between this version and the [Version of Record](#). Please cite this article as [doi: 10.1029/2023JE007851](https://doi.org/10.1029/2023JE007851).

This article is protected by copyright. All rights reserved.

Abstract

Migrating tides dominate the tropical climate on Mars and are known to reach high amplitudes during global dust events (GDE). In this study, we characterize the amplitude, phase and vertical wavelength of the diurnal and semi-diurnal migrating tides in Mars' lower atmosphere (up to 50km) by exploiting temperature vertical profiles retrieved from TIRVIM, an infrared spectrometer onboard the ExoMars Trace Gas Orbiter covering multiple local times. Observations from the Mars Climate Sounder onboard the Mars Reconnaissance Orbiter are used to complement the local time coverage when needed, and to estimate a seasonal trend to subtract from TIRVIM observations. We focus on two time periods in Martian Year 34, near $L_s=150^\circ$ and near $L_s=200^\circ$ (during the 2018 GDE). The characteristics of the migrating tides at $L_s=150^\circ$ agree very well with tidal theory: a downward propagation, amplitudes of typically 2–5K, and a larger vertical wavelength for the semi-diurnal compared to the diurnal mode. Comparisons with model predictions from the Mars Planetary Climate Model reveal an excellent agreement, except for a slightly different phase of the diurnal tide. During the GDE, the tide pattern changes spectacularly: the diurnal tide amplitude reaches 35K at 65°S and 17K at 50°N , being vertically trapped up to 10Pa. The semi-diurnal tide is maximum near $20\text{--}30^\circ\text{S}$ with an amplitude of 8–12K. The phase of this mode is tilted with latitude, which was not the case before the storm. This indicates a significant contribution of the asymmetric Hough modes due to hemispheric asymmetry in the dust distribution.

Plain Language Summary

Important temperature variations are observed in the Martian atmosphere at diurnal scale. Part of these variations are due to a phenomenon called migrating thermal tides, which take the form of global oscillations with periods that are diurnal, or fractions of a day (half a day period = semi-diurnal, a third of a day = ter-diurnal, etc). Using satellite observations sampling different local times on Mars, we separated these different components and derived their amplitude and phase (the local time at which these oscillations peak) in particular during the Global Dust Event that occurred in 2018. During this major storm, diurnal temperature variations reached 65K at high southern latitudes near 25km altitude between the late morning (minimum of temperature) and late evening (maximum of temperature). We also report on the characteristics of the semi-diurnal tide and even the ter-diurnal tide, which have been less studied during dust storms.

53 The phase of the semi-diurnal tide is not the same at all latitudes, which we interpret
54 as a consequence of the asymmetric dust distribution (more dust in the southern hemi-
55 sphere). Our results agree with predictions from a Global Climate Model, although some
56 small disagreements are found, calling for future improvements in the model.

57 1 Introduction

58 Thermal tides are the dynamical response of the atmosphere to diurnal solar heat-
59 ing. While they have a small amplitude on Earth, they dominate the tropical climate
60 on Mars, due to its much smaller atmospheric density. Tides are sorted in different cat-
61 egories according to their direction of propagation (eastward or westward), their zonal
62 wavenumber s and period per sol σ . Among them, migrating thermal tides are Sun-synchronous,
63 hence propagate westward with the Sun, with periods that are integer fractions of the
64 solar day. The main harmonics are the diurnal migrating tide (with a diurnal period and
65 a zonal wavenumber of one, ie $s = \sigma = 1$), referred to as DW1, followed by the semi-
66 diurnal migrating tide ($s = \sigma = 2$) SW2 and the ter-diurnal tide ($s = \sigma = 3$) TW3
67 (Forbes et al., 2020). The meridional and vertical structures of such tides are expected
68 to be a combination of Hough functions, as predicted from classical tide theory (Lindzen,
69 1970; Zurek, 1976; Wilson & Hamilton, 1996). A given harmonic response (DW1, SW2,
70 ...) can be decomposed in several modes (through the Hough functions), some of which
71 propagate vertically while others are vertically trapped. As they are thermally-forced,
72 tide amplitudes are expected to vary depending on dust and water ice cloud content (e.g.
73 Wilson & Richardson, 2000). In particular, a spectacular increase of the amplitude of
74 the DW1 tide at extratropical latitudes have been reported during Global Dust Events
75 (GDE) (e.g. Guzewich et al., 2014) and the amplitude of the SW2 harmonics was found
76 to be linked to the radiative effect of water ice clouds (Kleinböhl et al., 2013) and vertically-
77 extending dust forcing (Wilson & Hamilton, 1996; Steele et al., 2021).

78 These modes have been previously studied by a variety of instruments, from sur-
79 face pressure sensors ((where the SW2 signature is particularly clean, e.g. Leovy & Zurek,
80 1979)) to upper atmospheric density measurements (e.g. Lo et al., 2015). In this paper
81 we focus on tide signatures measured in the tropospheric temperature fields derived from
82 TIRVIM (Thermal InfraRed channel in honor of professor Vassilii Ivanovich Moroz), the
83 thermal infrared spectrometer of the Atmospheric Chemistry Suite (ACS) instrument
84 onboard the Trace Gas Orbiter spacecraft (Korablev et al., 2018; Guerlet et al., 2022).

85 Similar past investigations were mostly based on instruments mounted on Sun-synchronous
86 orbiters such as the Thermal Emission Spectrometer (TES) onboard the Mars Global
87 Surveyor (MGS) (Banfield et al., 2000; Guzewich et al., 2014) and the Mars Climate Sounder
88 (MCS) onboard the Mars Reconnaissance Orbiter (Lee et al., 2009). The identification
89 and characterization of the thermal tides from these data sets is inherently hampered
90 by their limited local time coverage (near 2–3 am and 2–3 pm). Combining in-track and
91 cross-track MCS limb observations (which provides observations at six different local times)
92 allowed Kleinböhl et al. (2013) and Wu et al. (2015) to partially address the aliasing is-
93 sues and derive the amplitude of the semi-diurnal migrating tides and several non-migrating
94 tides. However, unequal spacing of the six observations leads to very large uncertainties:
95 Kleinböhl et al. (2013) report uncertainties of 4–5K on the derived SW2 amplitude.

96 More recently, two other thermal infrared spectrometers onboard non-Sun synchronous
97 orbiters have allowed to even more precisely derive the tide amplitudes and phases, namely
98 from TIRVIM/TGO (Fan, Guerlet, et al., 2022) and EMIRS onboard the Emirates Mars
99 Mission (Fan, Forget, et al., 2022). Both studies focused on evaluating migrating tide
100 properties at $L_s=90^\circ$ during Martian Year 35 (for the TIRVIM study) and 36 (for the
101 EMIRS study). The nearly complete local time coverage of these two instruments yielded
102 unprecedented estimates of the phases of the tides, although it was found that in the case
103 of TIRVIM, aliasing between seasonal and local time sampling (TIRVIM covers the full
104 diurnal cycle over a martian month) impacted the determination of semi-diurnal tide prop-
105 erties. On the other hand, EMM can monitor all local times over ~ 10 sols, which allowed
106 the authors to identify and characterize for the first time the ter-diurnal mode in such
107 thermal infrared observations. In both studies, a good agreement was found with model
108 predictions except for a ~ 2 -hour shift in the phase of the diurnal mode. Continuing to
109 monitor and document the tides characteristics at other seasons is important to better
110 understand their forcing mechanisms and their link with the global circulation. In par-
111 ticular, extreme changes in the tide characteristics are expected during dust storms. TIRVIM
112 witnessed a Global Dust Event in 2018 during MY34, that has been already studied from
113 the MCS point of view but only at two local times. Indeed, Kleinböhl et al. (2020) re-
114 ported a strong increase in diurnal tide amplitude, reaching 29K at 60°S , but the authors
115 could not study other tide modes. On the other hand, Vlasov et al. (2022) studied the
116 global thermal structure of the Martian atmosphere during the MY34 GDE from TIRVIM
117 observations, but not specifically the tide characteristics.

118 In this paper, we complete these existing studies by constraining the amplitudes
119 and phases of the diurnal and semi-diurnal thermal tides from ACS/TIRVIM data ac-
120 quired at another season: we report on the tide characteristics observed in April-May
121 2018, near $L_s=150^\circ$ of Martian Year 34, and then in June-July 2018, during the global
122 dust event (GDE) of that year, around $L_s=200^\circ$. Compared to Fan, Guerlet, et al. (2022),
123 we hereby attempt to quantify and remove the seasonal variability component of TIRVIM
124 observations by using concomitant MCS ones. These observations, along with our method-
125 ology of tide decomposition and seasonal de-trending, are described in Section 2. Results
126 on tide characteristics are then detailed and discussed in Section 3 for the pre-storm con-
127 ditions, and in Section 4 for the MY34 global dust event. Comparisons with predictions
128 from the Mars Planetary Climate Model (PCM) are included in both these sections. Fi-
129 nally, we summarize our results and conclude in section 5.

130 2 Observations and method

131 2.1 TIRVIM observations

132 TIRVIM is a Fourier-transform spectrometer, part of the Atmospheric Chemistry
133 Suite (ACS, Korablev et al. (2018)). It is mounted on board the ExoMars Trace Gas Or-
134 biter (TGO), an ESA-Roscosmos satellite whose scientific campaign began in March, 2018.
135 While TGO is still operational, TIRVIM cryocooler stopped functioning in December,
136 2019. TIRVIM mostly operated in nadir geometry, where it recorded thermal emission
137 of Mars' surface and atmosphere with sufficient signal-to-noise ratio between 600 and $1,300\text{ cm}^{-1}$
138 and with a spectral resolution of 1.2 cm^{-1} . TGO lies on a near circular orbit at 400-km
139 altitude with an inclination of 74° . Its orbit design is such that the local time of TIRVIM
140 nadir observations drifted by 13 minutes earlier each sol. After 54 sols, a full coverage
141 of the daily cycle was achieved. We have developed an algorithm based on optimal es-
142 timation theory to simultaneously retrieve, from TIRVIM nadir spectra, the surface tem-
143 perature, the vertical profiles of the temperature between a few km and 50–55 km (2–
144 3 Pa), and the column optical depth of dust and water ice clouds (Guerlet et al., 2022).
145 The retrieved temperature profiles have a vertical resolution of typically 10 km (or one
146 atmospheric scale height) in the lower atmosphere and an even coarser resolution of 20 km
147 in the range 2–20 Pa. Details of our algorithm along with a cross-validation exercise of
148 the retrieved temperature profiles with those acquired by the Mars Climate Sounder (MCS)
149 can be found in Guerlet et al. (2022).

150 In this paper we consider vertical temperature profiles retrieved from TIRVIM data
151 acquired over two periods of Northern Hemisphere summer and autumn of Martian Year
152 (MY) 34. The first set corresponds to the first 45 sols of its operations, between March
153 13 and April 28 2018, ie from $L_s=142^\circ$ till $L_s=167^\circ$ of MY34. An issue with the stabil-
154 ity controller of the double pendulum movement was encountered on April 28 (and lasted
155 over a month), which is the reason for stopping our first selection at this date. Figure 1
156 (left panel) shows the coverage of these observations as a function of latitude and local
157 time. Over these 45 sols, almost a full coverage of the daily cycle was obtained. Only
158 local times between 7 AM and 10 AM are missing south of 20°N , and local times between
159 7 PM and 10 PM are missing north of 20°S . Latitudes south of 55°S are mostly missing
160 at all local times: spectra were of poor-quality in this area, due to cold surface temper-
161 atures (hence low signal and signal-to-noise ratio).

162 The second set was acquired during the global dust event of MY34. Initially, a dust
163 storm started locally on 2 June 2018 ($L_s=186^\circ$) near the equator, then moved southward
164 along Acidalia dust storm track and extended both northward and southward. This dust
165 event reached a mature phase and became planet-encircling from 21 June ($L_s=197^\circ$) on-
166 ward (Kass et al., 2020), which is thus chosen as the starting date of our selection of TIRVIM
167 data. On 15 July ($L_s=212^\circ$), an overheating event of TIRVIM detectors occurred and
168 the instrument had to be turned off for several weeks. Hence, 25 sols of TIRVIM obser-
169 vations are available during the peak of the global dust event, covering local times 3:30–
170 9:30 AM and 3:30–9:30 PM (for equatorial observations). The corresponding latitude ver-
171 sus local time coverage is shown in Figure 1.

172 2.2 Decomposition of thermal tide modes

173 Our aim is to constrain the migrating tide amplitudes and phases by exploiting the
174 retrieved temperature profiles acquired at various local times by TIRVIM. Zonal vari-
175 ations seen in a fixed local time reference frame can be the signature of stationary waves
176 or non-migrating tides. On the other hand, migrating tides are by definition zonally-symmetric
177 in a fixed local time reference frame ($m = s - \sigma = 0$). In the following we thus exploit
178 the zonally-averaged temperature, where stationary waves and non-migrating tides should
179 be averaged out so that we are left only with the zonally-symmetric component of ther-
180 mal tides (the $m=0$ modes). This approach has been used in a large number of studies
181 since the Viking epoch, and is similar to that used for instance by Kleinböhl et al. (2013).

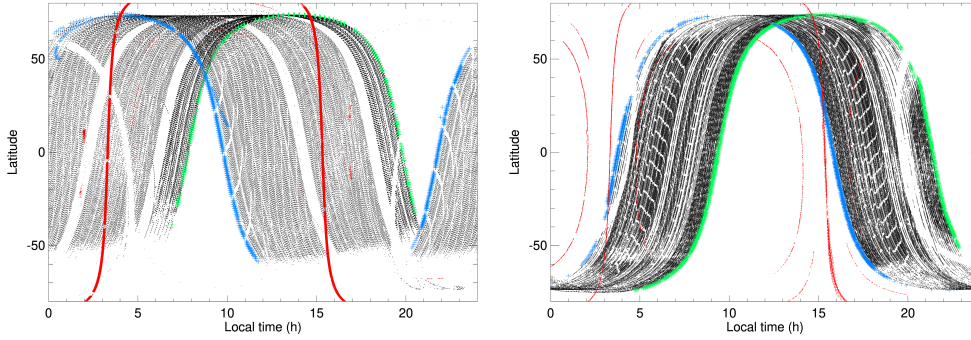


Figure 1. Latitude-local time coverage of individual TIRVIM observations, shown as black dots between Ls=142° and 167° (March 13 to April 28, 2018, left panel) and between Ls=197° and 212° during the global dust event of MY34 (21 June till 15 July, 2018, right panel). To give a sense of how time (Ls) flows, the first and last orbits are colored in green and blue, respectively. Red dots show the coverage of MCS data for the same time periods: most of them are "along-track" data, centered near 3 AM and 3 PM.

182 We proceed by binning these profiles in bins 45 minutes-long in local time, 5 or 10°-
 183 wide in latitude (see below), and 20°-wide in longitude. Examples of the latitude–longitude
 184 coverage for a given 45-minute bin is shown in Figure 2. Our nominal choice for the lat-
 185 itudinal bin width is 10°, which ensures a high enough number of observations within
 186 the bin (at least 10). We switch to a 5°-wide bin in regions of strong latitudinal temper-
 187 ature gradients, near the polar vortex, to limit the effect of mixing temperature varia-
 188 tions of different nature (both diurnal and meridional) if the latitudinal sampling is not
 189 uniform among different local time bins. We then take the zonal average of each (lat-
 190 itude, local time, pressure) bin. We retain only the bins with sufficient longitudinal cov-
 191 erage, ie. with at least 15 out of 18 longitudinal bins filled with temperature data.

192 For each latitude bin and pressure level, we assume that the local time variations
 193 of the zonally-averaged temperature can be split into three components: a daily aver-
 194 age temperature T_{avg} plus the modulations due to the DW1 and SW2 harmonics of the
 195 migrating thermal tides. During the GDE, we tested adding two other parameters to fit
 196 the ter-diurnal TW3 component, as justified in section 4.2.1. We thus fit the following
 197 function to the observations:

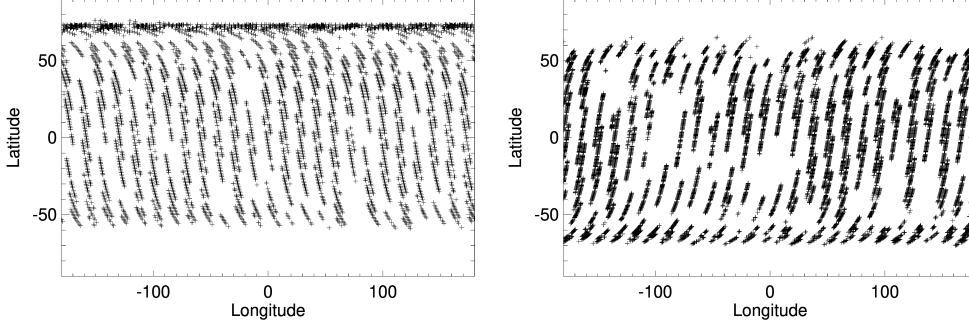


Figure 2. Longitude–latitude coverage of individual TIRVIM observations within a given 45-min long bin in local time. Left: for the bin 11:15 AM–12:00 AM, Ls between 142 and 167°; Right: for the bin 5:15 AM–6:00 AM, Ls between 197 and 212°.

$$T(t, \lambda, p) = T_{\text{avg}}(\lambda, p) + A_1(\lambda, p) \cos(t - \phi_1(\lambda, p)) + A_2(\lambda, p) \cos(2t - 2\phi_2(\lambda, p)) + A_3(\lambda, p) \cos(3t - 3\phi_3(\lambda, p)) \quad (1)$$

(only for the GDE case)

with $T(t, \lambda, p)$ the temperature at a given latitude λ , pressure level p and local time t ; A_1 , A_2 and A_3 the amplitudes of the diurnal, semi-diurnal and ter-diurnal modes, and ϕ_1 , ϕ_2 and ϕ_3 their phases. The quality of the fit to TIRVIM temperatures is assessed by computing a χ^2 value:

$$\chi^2(\lambda, p) = \sum_t \left(\frac{(T_{\text{TIRVIM}}(t, \lambda, p) - T(t, \lambda, p))}{\sigma(t, \lambda, p)} \right)^2 \quad (2)$$

with σ the standard deviation of uncertainty on the zonally-averaged retrieved temperatures, defined in section 3.4. Using equation 1 to fit the observations assumes that all the variability seen in the binned data at a given latitude and pressure level can be attributed to diurnal variations. However, as the local time sampling of TIRVIM data drifts with time (see Figure 1), our data set actually displays a combination of diurnal and seasonal or synoptic variations. If there are significant seasonal changes over a few tens of sols (a typical time interval needed to cover multiple local times with TIRVIM), the risk is then to wrongly interpret those seasonal or synoptic changes as local time variations. As discussed in Fan, Guerlet, et al. (2022), this could significantly impact the derived amplitude of the semi-diurnal tides from TIRVIM, due to the specifics of TGO’s orbit. Indeed, in the scenario where the temperature would regularly increase between

215 Ls=142° and 167°, then from TIRVIM point of view, this would be seen as two trends
216 of temperature increasing towards earlier local times, one from 7PM to 10AM and the
217 other from 7AM to 10PM (we recall that the instrument samples the atmosphere at two
218 local times twelve hours apart for each 2-hour long TGO orbit, see Fig. 1), creating a
219 "false" semi-diurnal tide signature. We present a way to mitigate this effect in the next
220 subsection.

221 **2.3 Seasonal de-trending from Mars Climate Sounder data**

222 To estimate the magnitude of seasonal changes over the course of the TIRVIM time
223 series considered here, we exploit temperature profiles obtained from the Mars Climate
224 Sounder (MCS).

225 MCS is a radiometer onboard the Mars Reconnaissance Orbiter (McCleese et al.,
226 2007) operating since 2006. It routinely records the thermal infrared emission of the mar-
227 tian atmosphere in limb and on-planet viewing geometry. Combining the thermal emis-
228 sion recorded at nadir, at different tangent altitudes in limb geometry, and in several chan-
229 nels covering the CO₂ band, allows the retrieval of temperature vertical profiles from 5
230 to 80 km with a 5 km vertical resolution (Kleinböhl et al., 2009). Due to the Sun-synchronous
231 orbit of MRO, in-track MCS data, acquired when the instrument views the limb in the
232 direction of spacecraft travel, are available at local times of ~3 AM and ~3 PM. Cross-
233 track observations, where the instrument views the limb perpendicular to spacecraft travel,
234 are also regularly done at ±1:30 around these two local times. In case of a too high opac-
235 ity along the line of sight (especially within the aphelion cloud belt or during dust storms),
236 limb retrievals cannot be done, which reduces the vertical coverage of the retrieved pro-
237 files to down to typically 10–50 Pa (Kleinböhl et al., 2013; Guzewich et al., 2012). Cross-
238 track observations are more impacted than in-track ones, as the latter further exploit planet-
239 viewing observations (for which the line-of-sight opacity is lower) to get complementary
240 constraints on the retrieved profiles. MCS temperature profiles are available on the at-
241 mospheres node of NASA's Planetary Data System. For our study, we extract available
242 MCS temperature profiles from version 5.2 in the intervals Ls=140–168° and from ver-
243 sion 5.3.2 for the GDE period (Ls=197°–212°). As we are interested in evaluating how
244 seasonal changes can impact TIRVIM nadir observations over 50 sols, we first convolve
245 MCS profiles with a gaussian profile with a full width at half maximum of one scale height,
246 to emulate TIRVIM coarser vertical resolution. We then bin these profiles in Ls (3°-wide

247 bins), latitude (10° -wide bins) and longitude (30° -wide bins) before computing the zonal
 248 average of the temperature for each latitude, Ls bin and pressure level, separately for
 249 the nighttime and daytime MCS data.

250 *2.3.1 Seasonal changes around $L_s=150^\circ$*

251 Considering first the $L_s=140\text{--}168^\circ$ period, we note that MCS temperatures show
 252 a warming seasonal trend at low and mid-latitudes, both at 3 AM and 3 PM (see Fig-
 253 ure 3). For instance, at 200 Pa, equatorial temperatures increased by $+12\text{K}$ both at 3 AM
 254 and 3 PM over this 45-sol period. This trend is even greater at high southern latitudes,
 255 as spring was nearing. On the other hand, high northern latitudes cooled down by $\sim 8\text{--}$
 256 12K as autumn was approaching. The seasonal trends estimated separately at 3 AM and
 257 3 PM differ slightly. This difference is in general smaller than the trend itself (compare
 258 for instance the $+10\text{K}$ nighttime trend and the $+8\text{K}$ daytime trend derived at 30 Pa at
 259 the equator), so that using an average of the afternoon and nighttime trends, while im-
 260 perfect in nature, should nonetheless reduce the seasonal bias of TIRVIM data. An ex-
 261 ception to this rule is found at high southern latitudes, south of 50°S where for pressures
 262 lower than 100 Pa, the 3 AM and 3 PM seasonal trends differ significantly (compare the
 263 rather constant 3 AM temperature at 30 Pa, $50^\circ\text{--}60^\circ\text{S}$, with the seasonal increase of $+5\text{ K}$
 264 at 3 PM at this latitude). This hints to a subtle interplay between seasonal and local time
 265 variations at this time of year, likely due to seasonal changes in the tide response as the
 266 southern hemisphere eastward jet evolves with season. This will have to be kept in mind
 267 when interpreting the results. We also notice that beyond $L_s=160^\circ$, seasonal warming
 268 occurs faster than in the range $140\text{--}160^\circ$, especially for pressures lower than 100 Pa. Hence,
 269 we choose to fit the MCS temperature anomalies with two linear trends (one for $L_s=140^\circ$
 270 to 158° , the other for $L_s=158^\circ$ to 170°), and use them to de-trend TIRVIM temperature
 271 profiles. Equation 1 is then applied to these de-trended temperatures to derive tide char-
 272 acteristics.

273 *2.3.2 MCS observations during the Global Dust Event of MY34*

274 During the global dust event period covered by TIRVIM ($L_s=197\text{--}212^\circ$), the at-
 275 mosphere warmed by typically 5 to 10K at 30 Pa (see Figure 4), except at high south-
 276 ern latitudes where a $+30\text{K}$ temperature increase was recorded at 70°S in the afternoon
 277 MCS data ($+20\text{K}$ at night). The bulk of the atmospheric warming would be due to ab-

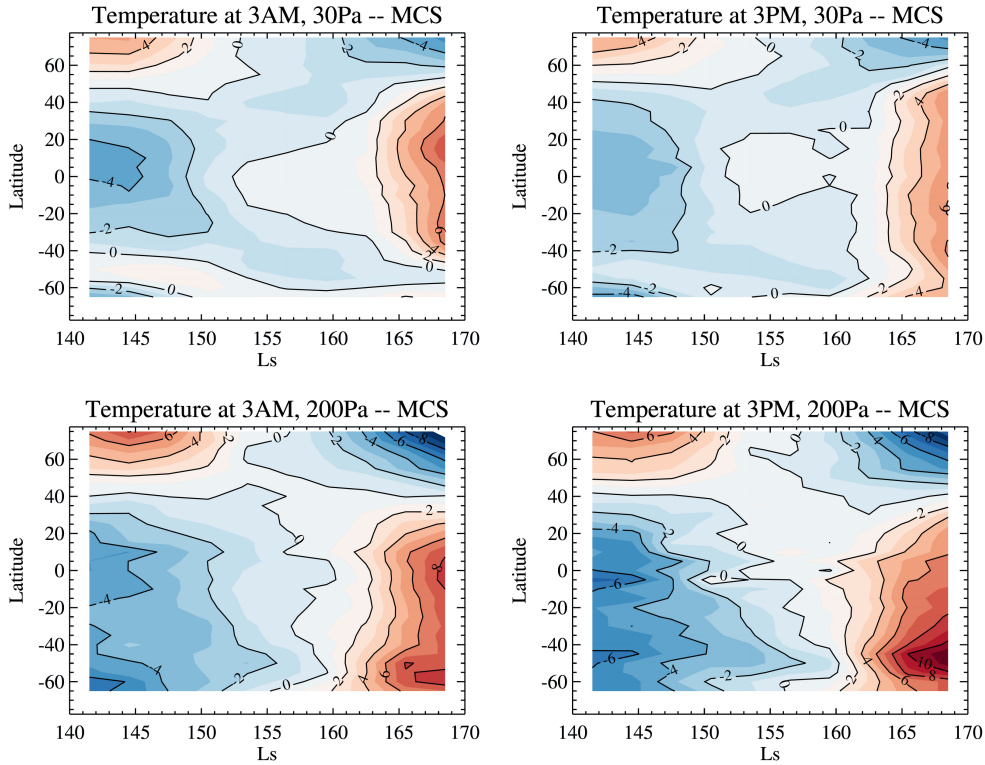


Figure 3. Anomaly (temporal average removed for each latitude bin) of the zonally-averaged temperature as recorded by MCS between $L_s=140^\circ$ and 168° , binned by 3° in L_s . The temperature anomalies are shown separately at 3 AM (left) and 3 PM (right) at two pressure levels (30 Pa, upper row and 200 Pa, lower row), with a contour interval of 2K.

278 sorption of solar radiation by dust; while the significant warming at high southern lat-
 279 itudes is probably caused by the intensification of the meridional circulation at that time,
 280 in response to strong radiative forcing of dust and large amplitude diurnal tides at high
 281 southern latitudes (Kleinböhl et al., 2020).

282 Similar to the pre-dust storm period, we fit the MCS trends with linear functions
 283 for each latitude bin and pressure level, de-trend TIRVIM data accordingly and apply
 284 equation 1. We note that the rate of temperature increase differs between day and night
 285 at high southern latitudes: at 70°S , afternoon temperatures warmed quickly from $L_s=197^\circ$
 286 to 206° and then only moderately increased, while it was the opposite for nighttime tem-
 287 peratures. We will thus treat with caution the results obtained south of 60°S , due to the
 288 complexity of these mingled diurnal and seasonal variations.

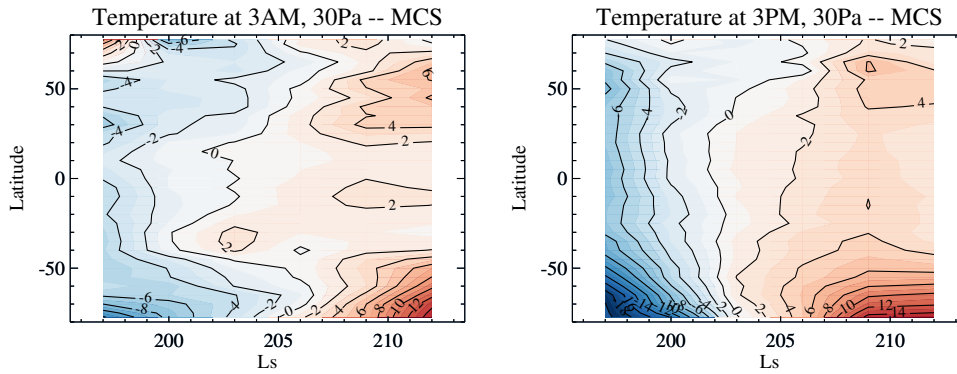


Figure 4. Anomaly (temporal average removed for each latitude bin) of the zonally-averaged temperature as recorded by MCS between $L_s=197^\circ$ and 212° , binned by 3° in L_s . The temperature anomalies are shown separately at 3 AM (left) and 3 PM (right) at 30 Pa, with contours drawn every 2K.

2.4 Difference in the methodology during the GDE

The local time coverage during the MY34 GDE ($L_s=197^\circ$ to 212°) is not as good as in the previous case study at $L_s=150^\circ$. Only half a martian day, or more precisely, two times 6 hours of local time, are covered over the 25 sols duration of this dataset (see Fig. 1). In order to slightly improve this point, we added MCS temperature profiles to our data set, providing additional information mostly near 3 am in the southern hemisphere and 3 pm in the northern hemisphere. We selected MCS data only within $L_s=210$ – 212° , in line with the L_s – local time coverage of TIRVIM data (see Fig. 1). A prerequisite of combining TIRVIM and MCS temperature profiles is to check that there is no bias between the two datasets. A thorough TIRVIM-MCS cross-validation exercise was done for the pre-storm period (Guerlet et al., 2022), showing excellent agreement between the two datasets. To illustrate that this is also the case during the GDE, we present in Fig. 5 examples of co-located TIRVIM and MCS temperature profiles near 45°S , 3am and 42°N , 3pm. The vertical atmospheric thermal structure retrieved from MCS shows several cases of temperature inversion that are well captured by TIRVIM, although with a coarser vertical resolution inherent to nadir sounding. Most of the difference between the two datasets fall within error bars (typically 2K) when TIRVIM coarser vertical resolution is taken into account. Hence in the following, MCS profiles are first vertically smoothed

307 (convolved with a one scale height FWHM gaussian function, see Fig. 5) before the bin-
 308 ning procedure.

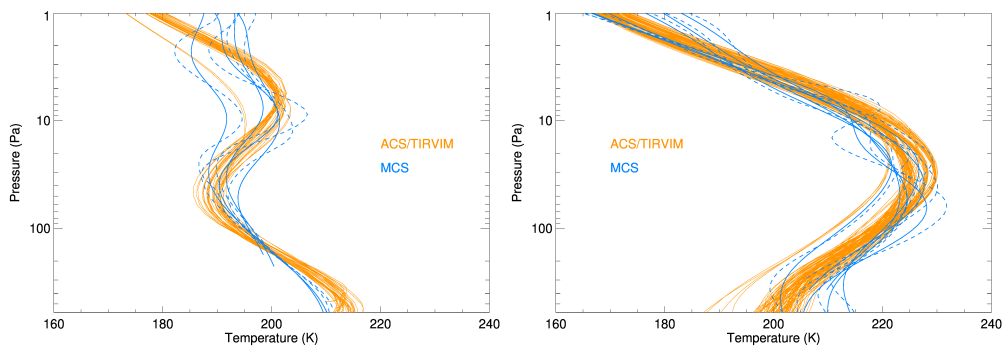


Figure 5. Examples of the good agreement between co-located MCS (in blue) and TIRVIM (in orange) temperature profiles near 45°S, 3AM (left) and 42°N, 3PM (right). Observations are defined co-located when they were acquired less than 30 minutes apart, 2° in latitude and 6° in longitude apart. Dashed blue lines show the MCS profiles on their native pressure grid while solid blue lines represent vertically smoothed MCS profiles (see text).

309 2.5 Mars global climate simulations

310 In following sections, we will also compare our results to simulations done with the
 311 Mars Planetary Climate Model (PCM, previously known as the Laboratoire de Météorolo-
 312 gie Dynamique Global Climate Model or LMD GCM), run with the MY34 dust scenario.
 313 We use the standard configuration of version 5 of the PCM, with a resolution of 64×48
 314 in latitude×longitude and run with 32 vertical layers, up to 122 km. Among improve-
 315 ments implemented since the work of Forget et al. (1999), the radiative impact of clouds
 316 are included (Madeleine et al., 2012) and the water cycle follows that described in Navarro
 317 et al. (2014). The model injects dust continuously in the first layer (regardless of time
 318 of day) and computes the vertical distribution of dust, while the total column of dust
 319 is forced (rescaled) to follow a daily climatology scenario based on MCS dust retrievals
 320 for MY 34 (Montabone et al., 2020). Temperature profiles are output 24 times per sim-
 321 ulated sol. We interpolate and extract model temperature profiles at the same latitudes,
 322 longitudes, local times and Ls as all individual TIRVIM soundings. We then emulate the
 323 effect of TIRVIM coarse vertical resolution and the influence of the *a priori* temperature
 324 profile \mathbf{T}_a used in the retrieval algorithm (which mostly influences the retrieved temper-

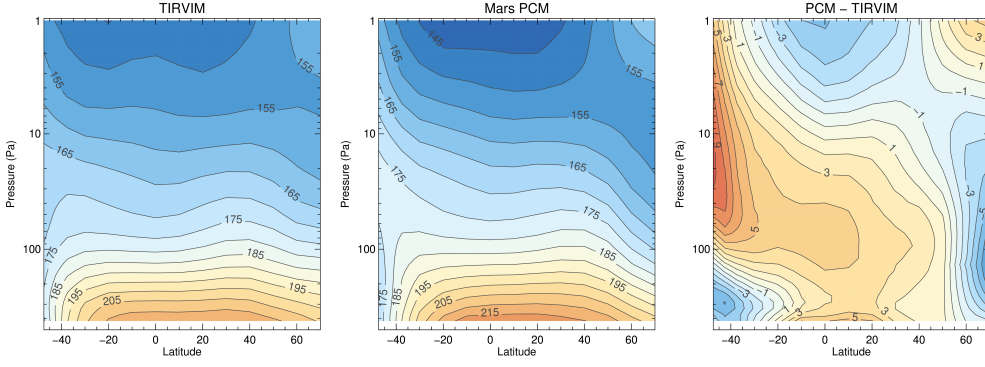


Figure 6. Latitude-pressure cross section of the diurnal mean temperature (T_{avg} in equation 1) from ACS/TIRVIM (left), from the PCM (middle), and the difference between model and observations (right). These figures correspond to $L_s \sim 150^\circ$ and were computed after a seasonal de-trending (see text for details).

325 ature profiles near the surface and at altitudes above the 5 Pa level) on the GCM pro-
 326 files by applying the following equation :

$$\hat{\mathbf{T}}_{\text{GCM}} = \mathbf{T}_a + \mathbf{A}_k(\mathbf{T}_{\text{GCM}} - \mathbf{T}_a) \quad (3)$$

327 with \mathbf{A}_k the averaging kernel matrix, representing the relative weight between the
 328 *a priori* and the observations, and accounting for the vertical resolution of the nadir ob-
 329 servations (see details in Guerlet et al., 2022). The $\hat{\mathbf{T}}_{\text{GCM}}$ profiles are binned in latitude,
 330 longitude and local time similarly as TIRVIM data, are zonally-averaged, and we per-
 331 form a seasonal de-trending based on the GCM temperature fields themselves at 3 AM
 332 and 3 PM, to mimic the de-trending procedure done on TIRVIM data. We then apply
 333 equation 1 to this binned data set to extract the thermal tides amplitudes and phases.

334 3 Thermal structure and tides for $L_s = 150^\circ$

335 3.1 Overview of the thermal structure

336 We first present an overview of the thermal structure obtained at $L_s = 150^\circ$. The
 337 latitude-pressure cross section of the fitted diurnal mean temperature (T_{avg} in equation 1)
 338 is shown in Figure 6. At this season, temperatures in the lower atmosphere ($p > 100$ Pa)
 339 are maximal between 20°S and 40°N and decrease sharply towards high southern lati-

340 tudes (end of winter conditions) and smoothly towards high northern latitudes (end of
341 spring). For instance, at 200 Pa, the daily averaged temperature derived from TIRVIM
342 decreases from a maximum of 197K at the equator to 174K at 50°S, 193K at 50°N and
343 189K at 70°N. Overall, temperatures from the model are in good agreement with the ob-
344 servations : differences between the two lie within ± 4 K for most of the latitude-pressure
345 domain. We note that the Mars PCM predicts steeper equator-to-pole gradients in the
346 lower troposphere, with for instance a minimum temperature of 170K at 50°S for a max-
347 imum temperature of 200K near the equator at 200 Pa.

348 At higher altitudes, the daily averaged temperatures are characterized by a tongue
349 of warmer air at mid- and high southern latitudes, as adiabatic warming from the de-
350 scending branch of the Hadley circulation cells takes place. Between ~ 5 and 100 Pa, near
351 40-50°S, the PCM predicts a significantly stronger warming than that observed. This observation-
352 model mismatch might reflect inadequacies in the model, such as an erroneous dust ver-
353 tical distribution and/or a too strong meridional circulation in the Mars PCM at this
354 season. However, we recall that at 40–50°S, the seasonal de-trending based on MCS data
355 applied to TIRVIM retrievals is quite uncertain, due to different daytime and nighttime
356 seasonal trends seen in MCS temperatures. Part (3K out of 4K) of the PCM-TIRVIM
357 mismatch could thus be attributed to uncertainties (of the order of 3 K) in de-trending
358 the observations.

359 3.2 Overview of local time variations

360 The zonally-averaged temperature variations with local time and latitude are shown
361 at three pressure levels in Figure 7. At low altitudes / high pressure levels (200 Pa), the
362 temperature is found maximum near 10°S and 3PM (205K). Peak-to-peak local time vari-
363 ations reach an amplitude of ~ 12 K. Apart from the difference in equator-to-pole gra-
364 dients mentioned above, the Mars PCM temperatures are in good agreement with TIRVIM
365 and also exhibit a local maximum near 3 PM at low latitudes.

366 At middle altitudes (30 Pa, approximately 30 km above the areoid), the diurnal
367 variations in temperature reveal a different pattern. Near the equator, the temperature
368 is found to be maximum near 3 AM and minimum near 7 PM. This feature of warm night-
369 time temperatures at this altitude is well known and is a manifestation of the vertically
370 propagating nature of the diurnal thermal tide in the tropics (Lee et al., 2009). The fact

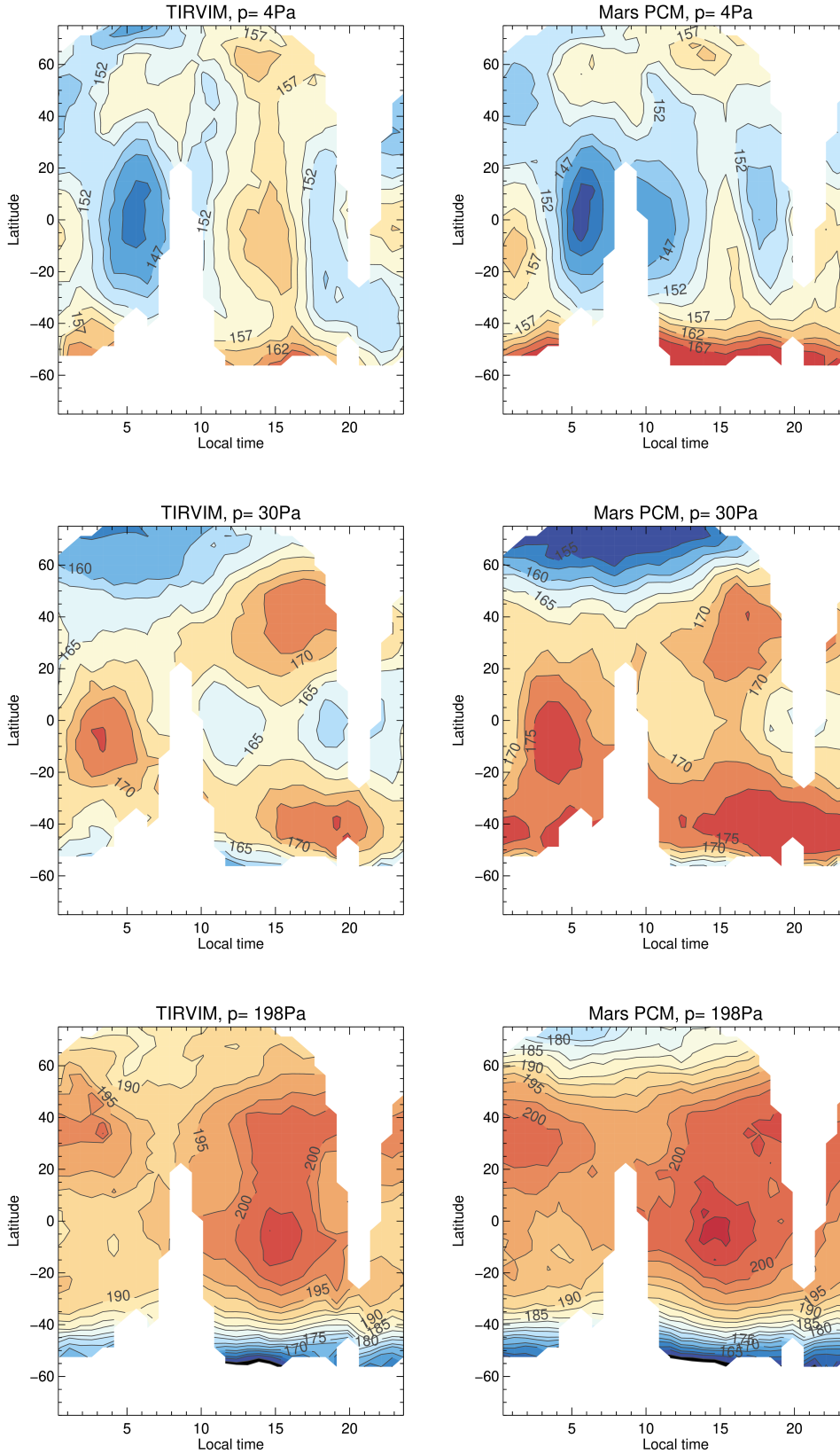


Figure 7. Zonal mean temperature with latitude and local time at 4 Pa (top), 30 Pa (middle) and 200 Pa (bottom), at $L_s \sim 150^\circ$. The left column corresponds to ACS/TIRVIM observations, the right column to the Mars PCM simulations, sampled at ACS/TIRVIM latitudes, longitudes, times and convolved to ACS/TIRVIM vertical resolution (\hat{T}_{PCM} in equation 3). To generate this figure, the data was binned by 5° in latitude and 30 minutes in local time. Contours are drawn every 2.5K (labeled every 5K).

This article is protected by copyright. All rights reserved.

371 that these two temperature extrema are not separated by 12 hours is a first hint that
372 the thermal field is also influenced by a semi-diurnal tide (note that a second local tem-
373 perature minimum is located near noon), as we will see in the next section. The mod-
374 eled temperature field exhibits a similar diurnal trend at low latitudes, although with
375 systematically warmer temperatures. At higher latitudes, the temperature is found to
376 be maximum near 3–8 PM at both 40°N and 40°S, with a rather symmetric structure
377 about the equator. In the Mars PCM, the local maximum near 45°S at 6PM is signif-
378 icantly warmer than its northern counterpart, and the high northern latitudes are also
379 much colder than that observed by TIRVIM: this reflects the overall PCM-TIRVIM dis-
380 crepancy in meridional trends seen in the diurnal average of the temperature discussed
381 earlier (see figure 6).

382 At low pressures (4 Pa, nearly 50 km altitude), the thermal structure is more com-
383 plex. The general trend of decreasing temperature from equator-to-pole is absent at this
384 pressure level, and is replaced by a family of local temperature extrema. Indeed, the cold-
385 est temperatures are not found at high latitudes (contrary to lower altitudes) but at the
386 equator, at 6 AM (both in the observations and the Mars PCM). A semi-diurnal pat-
387 tern is also clearly seen near the equator. To go beyond this qualitative analysis, we dis-
388 cuss below the amplitudes and phases of the migrating thermal tides and how well they
389 are reproduced in the model.

390 3.3 Thermal tides at the equator

391 Both the diurnal and semi-diurnal tides are expected to have significant amplitudes
392 near the equator. As a case study, we detail below the results regarding the equatorial
393 bin (-5°; +5°). The observed temperature diurnal anomalies and the fitted diurnal and
394 semi-diurnal components of the migrating tides at all pressure levels are presented in Fig-
395 ure 8. At the equator, the amplitude of the diurnal tide is found to be locally maximum
396 near 50 Pa and 3 Pa with values of 4.9 K and 5.2 K, respectively. The semi-diurnal tide
397 is maximum over the range 2–10 Pa, where its amplitude is in the range 4–5.5 K. Ex-
398 amples of best fits to TIRVIM temperatures, along with the different contributions of
399 the diurnal and semi-diurnal modes, are shown in Figure 10 at 50 and 10 Pa. Our re-
400 sults clearly assess the downward phase propagation of both the diurnal and semi-diurnal
401 tides, which is consistent with upward group velocity for inertia-gravity waves and com-
402 plies with tidal theory (Lindzen & Chapman, 1969; Forbes, 1995). We also derive a much

403 longer vertical wavelength for the semi-diurnal tide compared to the diurnal tide, which
 404 is also expected. Corresponding vertical wavelengths amount to 4.5 scale heights (H) for
 405 the diurnal tide and 7.8 H for the semi-diurnal tide (see Fig. 9). These values are very
 406 close to that predicted by the Mars PCM : 4.8 H for the diurnal mode, 7.8 H for the semi-
 407 diurnal mode, increasing to 9.6 H if we consider the model results on their own latitude,
 408 longitude, local time and pressure grid instead of the co-located and vertically convolved
 409 model outputs.

410 A characteristic feature of the diurnal tide not well captured by TIRVIM is the ex-
 411 pected large amplification of the vertically-propagating component of tide with altitude,
 412 as atmospheric density exponentially decreases. This is well visible in the amplitudes de-
 413 rived from the modeled temperature field at the native vertical resolution of the Mars
 414 PCM (see the central row of Figure 8), where the amplitude of the diurnal tide reaches
 415 10–12K at 1–2 Pa. Amplitudes of 6–12K have previously been reported at this pressure
 416 level from MCS data analysis (Lee et al., 2009; Kleinböhl et al., 2013; Steele et al., 2021),
 417 however, in TIRVIM retrievals, the amplitude of the diurnal tide seems to decrease above
 418 the 3 Pa level. This apparent disagreement is an example of a shortcoming in TIRVIM
 419 nadir observations: above the ~ 5 Pa pressure level, the information content decreases
 420 and the retrieved temperature profile smoothly goes back to the *a priori* profile. TIRVIM
 421 vertical resolution is also coarser at this pressure range (1.5 to 2 scale height), which leads
 422 to an underestimation of the vertical oscillations that characterize the tides.

423 When TIRVIM information content is taken into account, the amplitudes of the
 424 diurnal and semi-diurnal tides derived from $\hat{\mathbf{T}}_{\text{PCM}}$ are in fair agreement with TIRVIM
 425 ones (see the bottom row of Figure 8), although we find a slightly stronger diurnal tide
 426 at 50 Pa in TIRVIM data compared to $\hat{\mathbf{T}}_{\text{PCM}}$. This result is considered robust, as the
 427 amplitude of the tide at 50 Pa in the Mars PCM is the same whether we consider \mathbf{T}_{PCM} ,
 428 $\hat{\mathbf{T}}_{\text{PCM}}$ or even the "raw" model outputs at $\text{Ls}=150^\circ$ on their native latitude, longitude,
 429 pressure and local time grid (ie. without selecting profiles co-located with TIRVIM ob-
 430 servations nor any vertical smoothing). The amplitude of the semi-diurnal tide is found
 431 to be similar between TIRVIM and the Mars PCM, except that our derived amplitude
 432 is stronger than the modeled one for $p < 10$ Pa. Actually, the semi-diurnal tide amplitude
 433 derived from TIRVIM is similar to the one in the Mars PCM obtained without vertical
 434 smoothing. We note however that the difference between the two modeled fields (ver-
 435 tically smoothed or not) is small in the case of the SW2 amplitude, owing to its larger

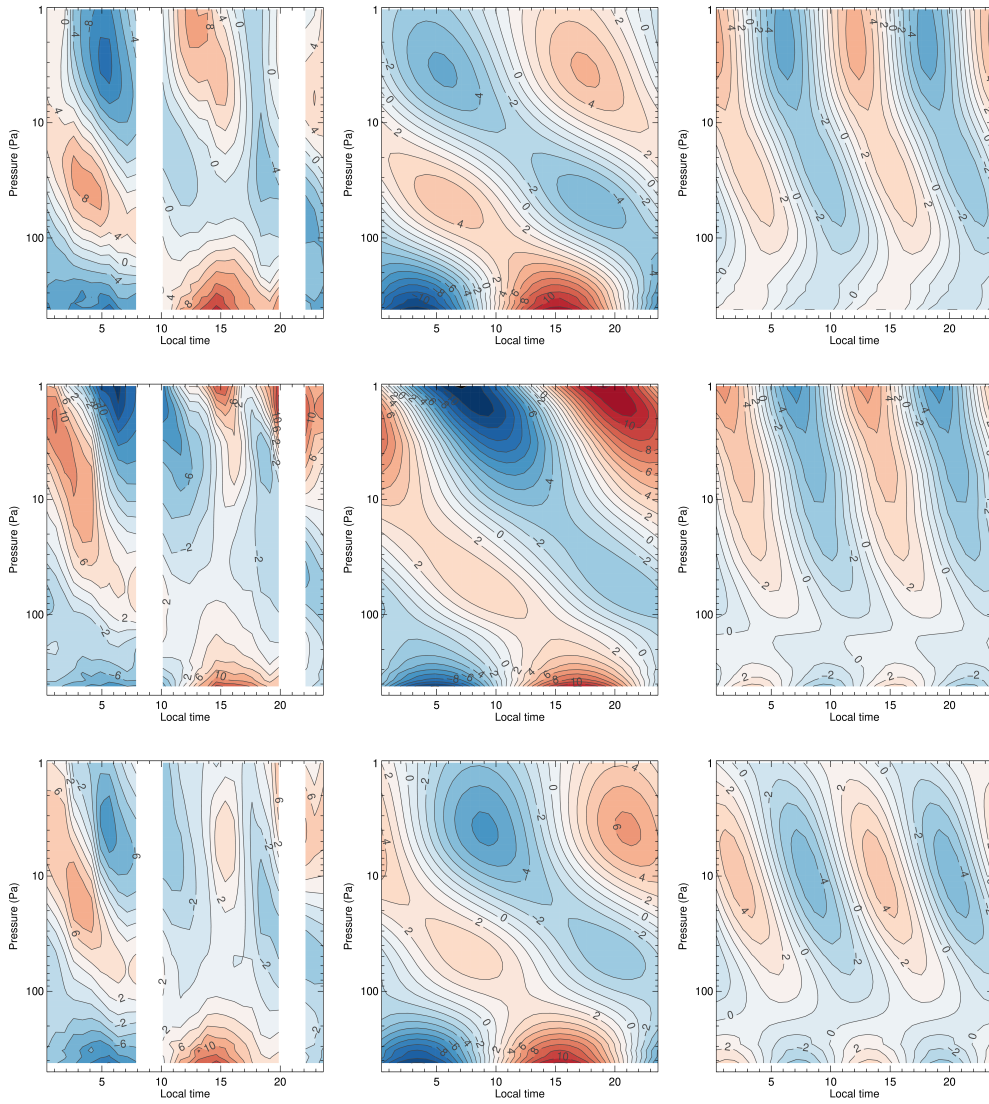


Figure 8. Left: Diurnal anomaly of the zonally-averaged temperature in the bin $(-5^{\circ}, 5^{\circ})$ at $L_s \sim 150^{\circ}$; middle: reconstructed diurnal mode of the migrating thermal tides from the fitted parameters in eq. 1; right: reconstructed semi-diurnal mode. The top row corresponds to ACS/TIRVIM retrieved temperatures, the middle row to predictions by the Mars PCM sampled at TIRVIM latitudes, longitudes and times on its native vertical grid, and the bottom row shows the same model results convolved to TIRVIM vertical resolution (\hat{T}_{PCM} in equation 3).

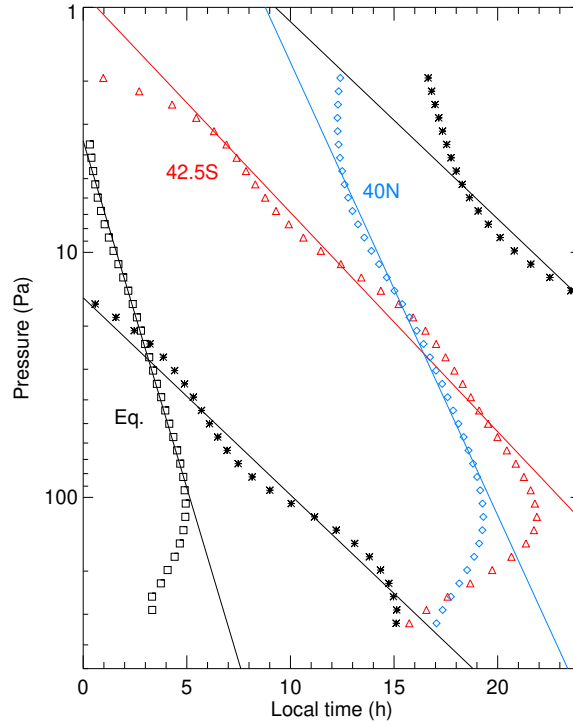


Figure 9. Phase of the diurnal (black stars) and semi-diurnal mode (black squares) at the equator, with pressure, at $L_s=150^\circ$. The vertical wavelength is estimated from linear fits, shown as solid lines. Phases of the diurnal mode for the bin 40N (blue diamonds) and 42.5S (red triangles) are also shown for comparison.

436 vertical wavelength. Finally, note that near 1–5 Pa, the semi-diurnal tide amplitude de-
437 rived from TIRVIM at the equator is commensurate, or even greater, than the diurnal
438 mode. This is not the case in the PCM results, where the DW1 tide amplitude is greater
439 than that of SW2.

440 The seasonal de-trending has an important effect: without it, the amplitude of the
441 semi-diurnal tide derived from TIRVIM would amount to 6.4K at 10 Pa (instead of 3.8K).
442 That is easily explained : as the background seasonal temperature increases over the course
443 of the 45 sols considered here (see fig. 3), and as TIRVIM acquired data at two local times
444 12 hours apart per TGO orbit (drifting in local time with Ls), this seasonal increase can
445 be wrongly interpreted as a warming occurring with local time, with two extrema per
446 day: in other words, seasonal warming is aliased with the semi-diurnal tide mode. This
447 aliasing effect was also reported by Fan, Guerlet, et al. (2022), who analyzed TIRVIM
448 observations near Ls=90° of MY35 without seasonal de-trending. Removing seasonal trends
449 before decomposing the tide harmonics yields a more realistic amplitude of the semi-diurnal
450 tide.

451 Regarding the phases of the tides, and taking 30 Pa as an *ad hoc* reference pres-
452 sure level, the temperature maximum associated with the diurnal tide is found to occur
453 at 4:30 AM in the observations and to occur slightly later, near 6:00 AM, in the mod-
454 eled field \hat{T}_{PCM} (or 5:40 AM in the raw model outputs). Such a $\sim 1\text{h}30\text{min}$ phase shift
455 between model and observations was also reported by Fan, Guerlet, et al. (2022) near
456 Ls=90° of MY35 and is currently under investigation. It could be related to unrealistic
457 aerosol vertical distribution (hence radiative forcing), both for dust and water ice clouds.
458 Indeed, at Ls= 150°, water ice clouds likely account for a significant part of the thermal
459 forcing (Haberle et al., 2019; Wilson et al., 2014). Another possible shortcoming is re-
460 lated to regional circulations, or topography-related circulations, not fully resolved by
461 the PCM. We also note that at this season, topographically-generated Kelvin waves are
462 known to interfere (destructive or constructive interferences) with the Sun-synchronous
463 tides (Wilson & Hamilton, 1996); studying these tides, their interactions, and how well
464 they are represented in the Mars PCM is deferred to future studies. Regarding the phase
465 of the semi-diurnal tide, we find an excellent agreement between model and observations
466 (less than half an hour difference, which is of the order of our bin size, hence not signif-
467 icant). Should we not de-trend the TIRVIM temperatures, we would find a 2h40min phase
468 difference between model and observations, similar to the 3-hour phase shift reported

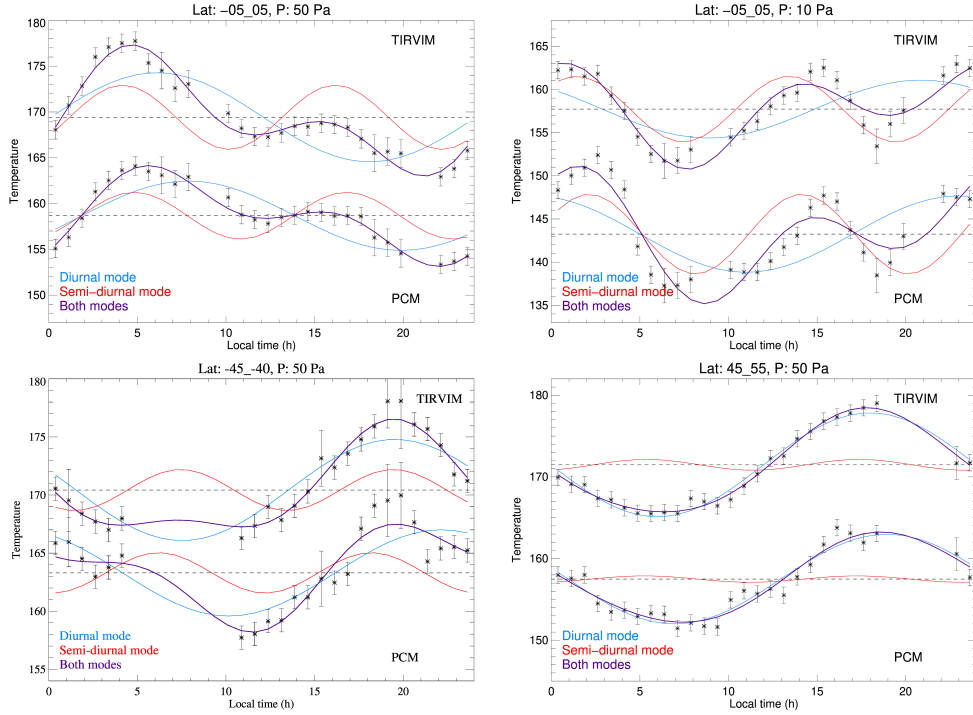


Figure 10. Zonally-averaged temperature as a function of local time as measured by TIRVIM (or computed from \hat{T}_{PCM} , shifted by -15K in each panel) at $L_s \sim 150^\circ$, shown as black stars at different latitude bins and pressure levels, as labeled. The fitted diurnal mean temperature is shown as a horizontal dashed line while the colored lines represent the fitted contributions from the diurnal (in blue) and semi-diurnal (in red) modes. Best fits to the data are shown in purple.

by Fan, Guerlet, et al. (2022) for the semi-diurnal tide at $L_s = 90^\circ$ that these authors derived from their TIRVIM analysis with no seasonal de-trending.

3.4 Comments on uncertainty estimates

Uncertainties on the derived tide amplitudes result from a combination of several factors: from measurement errors on the retrieved temperatures; uncertainties due to the incomplete local time coverage; from errors on computing the zonal averages (due to uneven sampling in latitude within a bin, or in longitude among the bins); and from seasonal trends mingled with local time variations that are not perfectly accounted for. The observational precision (not accuracy) is estimated to $0.5\text{--}1\text{K}$ and that on the seasonal de-trending is estimated to $1\text{--}2\text{K}$ depending on latitude, by looking at the differences between the 3 AM and 3 PM trends derived from MCS. Setting a nominal $1\text{-}\sigma$ uncertainty

480 of 1.5K for the zonally-averaged temperature thus seems reasonable. If the zonal cov-
481 erage is incomplete (we allow for one to three bins out of 18 to be missing), we artifi-
482 cially increase this value by quadratically adding a fraction of the variance among the
483 longitude bins at a given latitude, as there is a risk that strong waves (non-migrating tides)
484 are not fully cancelled and contribute to the averaged temperature.

485 The resulting reduced χ^2 values are close to unity (ranging between 0.5 and 1.5)
486 for all latitude bins for $p > 10$ Pa, and residuals are also smaller than 1.5K, which sug-
487 gests that these measurement uncertainty values are of the right order of magnitude. Note
488 that before seasonal de-trending, the χ^2 values were up to four times larger at low lat-
489 itudes and near 50°S , which re-enforces the necessity of this approach. The quality of
490 the fit nonetheless decreases towards lower pressure levels, reaching on average a χ^2 of
491 2.5 at 2 Pa. Indeed, residuals of typically 2K are present at low pressure levels, which
492 origin is not clearly established but is likely due to imperfect seasonal de-trending.

493 Given these observational uncertainties, the formal error on the fitted tide ampli-
494 tudes are of the order of 0.3–0.4K. However, this error is underestimated for several rea-
495 sons. Firstly, it is important to note that the tide amplitude themselves are expected to
496 vary over the course of the 45-sol period considered here (between sol 304 and 349). For
497 instance, considering the "raw" PCM outputs at sols 304, 319, 334 and 349, we find that
498 the diurnal tide amplitude at the equator changes by typically 1K (up to 2K for $P < 10$ Pa),
499 and that of the semi-diurnal tide by 0.5K (1K for $p < 20$ Pa), among these 4 selected sols.
500 Secondly, we note that a ter-diurnal thermal tide exists in the "raw" PCM outputs, with
501 amplitudes in the range 0.2 to 0.6K for pressures lower than 30 Pa. However, this mode
502 is not detected neither in TIRVIM nor in the $\hat{\mathbf{T}}_{\text{PCM}}$ fields when we add it in Eq. 1, con-
503 firming that even without any measurement error, the uncertainty on tide amplitudes
504 due to uneven spatio-temporal sampling is at least 0.6K. Fan, Forget, et al. (2022) did
505 detect the ter-diurnal mode using temperature profiles derived from another nadir-viewing
506 spectrometer, EMIRS, onboard the Emirates Mars Mission. The authors could reach a
507 higher precision thanks to the observing scheme that acquires observations at all local
508 times within a few sols only. Finally, we can also estimate the precision on tide ampli-
509 tudes by comparing that derived from the Mars PCM temperature field but sampled on
510 TIRVIM observational grid versus the temperature on the regular model grid on a given
511 sol, to evaluate the impact of incomplete spatio-temporal coverage as well as imperfect
512 seasonal de-trending. This difference is of the order of 1K for $p > 20$ Pa and increases to

513 2K at 1–3 Pa. The latter values are thus taken as our precision estimates for tide am-
514plitudes derived from TIRVIM.

515 In addition to these precision values, one has to keep in mind the poorer accuracy
516 of the observations at low pressure levels, due to the limited information content and coarse
517 vertical resolution. Absolute tide amplitudes derived from nadir observations can be un-
518 derestimated by a factor of 2 for $P < 10$ Pa as discussed in the previous section. However,
519 when comparing similar quantities (eg. \hat{T}_{PCM}), a precision of ~ 1 –2K on tide amplitudes
520 should nonetheless be reached.

521 3.5 Tide amplitudes and phases at all latitudes

522 Amplitudes and phases of both harmonics of the migrating tides are reported in
523 Fig. 11 as a function of latitude and pressure. We focus here on the meridional and ver-
524 tical structure of the tide harmonics, which can be represented by a combination of Hough
525 functions, according to classical tidal theory. In the tropics (15S to 20N), the DW1 sig-
526 nature is characterized by a vertically propagating component with downward phase prop-
527 agation and amplitudes of typically 3–4K. This meridional structure is a characteristic
528 feature of the (1,1) Hough function that corresponds to the main vertically propagat-
529 ing component of DW1, peaking at the equator and dominating at latitudes $< 30^\circ$. At
530 high latitudes ($> 60^\circ$), classical theory predicts a domination of vertically-trapped Hough
531 modes that are typically amplified within the westerly jets, and for which the temper-
532 ature response is effectively confined to the height range of dominant (aerosol) thermal
533 forcing. At mid-latitudes (40–50°), the diurnal tide would be both influenced by these
534 high latitude vertically-trapped Hough modes, and by the extra-tropical part of the (1,1)
535 vertically-propagating mode. The (1,1) mode indeed has significant negative nodes peak-
536 ing at 30° latitude (see for instance Fig. 2 in Wu et al., 2021). Here we report two dis-
537 tinct signatures at mid-latitudes depending on the considered hemisphere. On the one
538 hand, at latitudes 30–50°S, the DW1 signature exhibits downward phase propagation,
539 shifted by about 14 hours compared to the equator, with amplitudes of 2–3 K. The ver-
540 tical wavelength derived near 40°S and at the equator is similar and amounts to 4.8 H
541 (see also Fig. 9). This implies that the leakage of the tropical (1,1) Hough mode is clearly
542 dominant in the winter hemisphere, and that the vertically-trapped modes do not influ-
543 ence significantly the mid-latitudes at this season. On the other hand, near 30–60°N, al-
544 though we do report a downward phase propagation behavior as well, the vertical wave-

545 length is found to be larger : it ranges from 10 H (at 40°N) to 14 H (at 60°N). The tide
546 amplitude is also larger (4-6K) and peaks near 45-50° latitude. This suggests a compe-
547 tition between several Hough modes at summer mid-latitudes. Such a north-south asym-
548 metry in the vertical wavelength of DW1 in TIRVIM observations indicate differences
549 in tidal forcing (radiative forcing by aerosols for instance) and/or point to an alteration
550 of the meridional structure of the Hough functions by the background zonal mean wind
551 (classical tide formalism assumes no background zonal wind). These hypotheses remain
552 to be explored quantitatively. On the other hand, the DW1 phase structure in the Mars
553 PCM (on its native grid or considering \hat{T}_{PCM}) appears a) more symmetric about the equa-
554 tor and b) dominated by the (1,-2) Hough mode in particular in the northern hemisphere,
555 with a maximum amplitude at 60°N and an almost constant phase from the surface to
556 p=10 Pa at this latitude.

557 Regarding the semi-diurnal harmonic, we first caution that the tide amplitudes de-
558 rived from ACS/TIRVIM poleward of 40°N are small (less than 1K in general), which
559 results in poor confidence in the determination of its phase. Furthermore, we note strong
560 differences in the tide phases derived at high latitudes between the Mars PCM on its na-
561 tive pressure grid at one sol (318) and the ones estimated from \hat{T}_{PCM} sampled at TIRVIM
562 locations, local time and Ls. This implies that estimating the phase of SW2 is very sen-
563 sitive to the observation scheme at latitudes poleward of 40°, and we cannot interpret
564 these results. On the other hand, the broad equatorial maximum (in amplitude) of SW2
565 between 30°N and 30°S seems a robust feature and is similar in TIRVIM and the Mars
566 PCM. It shows slow downward propagation, corresponding to the (2,2) Hough mode that
567 is expected to dominate the SW2 tide structure.

568 Finally, we note that the overall latitudinal pattern of the thermal tide is not strictly
569 symmetric about 0° but is slightly shifted towards the southern hemisphere, with local
570 maximum amplitudes of both the diurnal and semi-diurnal tides centered at 5-10°S. This
571 feature is also present in the Mars PCM simulations and is also predicted by other cli-
572 mate models. Indeed, using MarsWRF, Lee et al. (2009) reported a seasonal dependence
573 of both the amplitude and the location (in latitude) of the peak of the 3pm-3am tem-
574 perature difference, being maximum and centered near 15°S at Ls=90°, minimum and
575 centered near 15°N at Ls=270°, and centered at 0° latitude at Ls=0° and 180°. Our anal-
576 ysis at Ls=150° matches well this prediction. Another GCM study (Wilson & Hamilton,
577 1996) also noted that the vertically propagating components of the tide harmonics tend

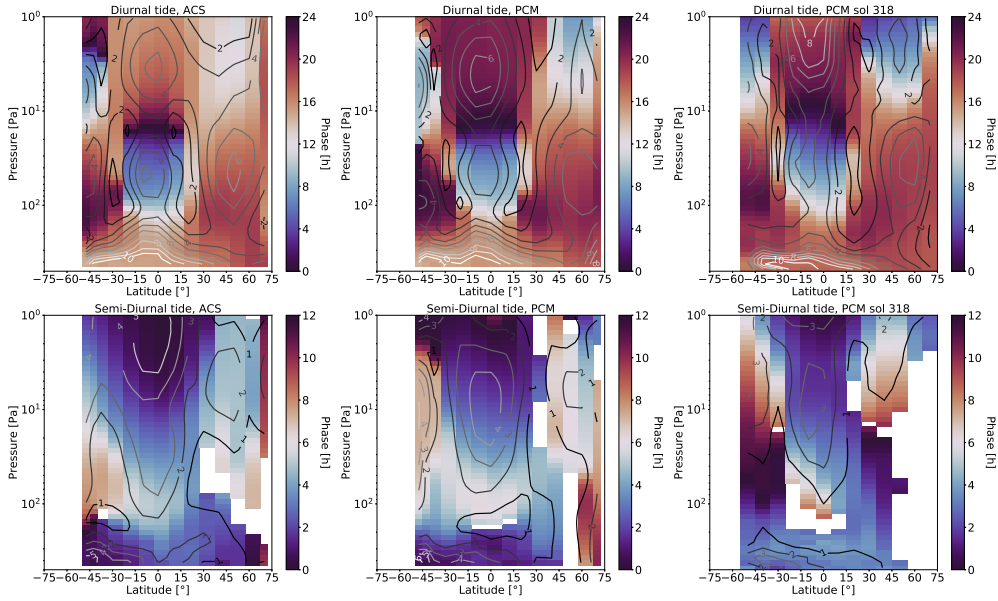


Figure 11. Phase (color, in hours) and amplitude (contour, in Kelvin) of the two main migrating tide harmonics at $L_s \sim 150^\circ$ (top row: diurnal, bottom row: semi-diurnal harmonic). The left column corresponds to ACS/TIRVIM temperatures, the middle one to \hat{T}_{PCM} and the right one to the Mars PCM on its native latitude, longitude and pressure grid at sol 318. Blank areas indicate regions where the derived SW2 tide amplitude was less than 0.5K, making phase determination unreliable.

578 to be ducted into the winter hemisphere. Classical tide theory predicts modes (Hough
 579 functions) that are centered at the equator, but this framework assumes zero background
 580 zonal wind. In the Earth atmosphere, the tide's amplitude and phase have been shown
 581 to be very sensitive to the absolute vorticity, ie. the sum of the Coriolis parameter and
 582 the relative vorticity, linked to latitudinal wind shears in the mean zonal wind (McLandress,
 583 2002). Although the Coriolis parameter is null at the equator, this is not the case of the
 584 absolute vorticity, due to zonal wind shears: as a result, the dynamical equator is not
 585 centered at zero latitude throughout the year, but is slightly ducted into the winter hemi-
 586 sphere. This might explain why the maximum tides' amplitudes also follow such a lat-
 587 itudinal trend with seasons.

3.6 Comparisons to previous observations and discussion

Comparison with previous nadir soundings, for this specific season, are limited. From TES aerobraking data, Banfield et al. (2000) estimated the amplitude of the diurnal tide to be of the order of 4K at an altitude of 3–4 scale height, at 40°S for $L_s=180^\circ$ during MY23. This is similar to the one derived here by TIRVIM at $L_s=150^\circ$ and 30 Pa (~ 3 scale heights). Unfortunately, TES aerobraking data were too sparse to correctly determine the tides' characteristics at low latitudes (Banfield et al., 2000). Using TES nadir observations from the nominal mission, acquired near 2am and 2pm, Banfield et al. (2003) performed a wave mode decomposition. However, with only two local times, the thermal tides are aliased and the amplitude and phase of the sun-synchronous diurnal tide cannot be derived properly.

Regarding limb measurements, MCS data available at this season and same martian year (MY34) were almost exclusively acquired near 3 am and 3 pm (see Figure 1). In a previous study, a comparison of TIRVIM temperature profiles with a set of co-located data from MCS (acquired at \pm one sol, less than 3° away in latitude, 6° away in longitude and 30 minutes away in local time) has revealed an excellent agreement between the two data sets, shown in Guerlet et al. (2022) as part of a cross-validation exercise. From this study, the 3pm–3am peak-to-peak temperature difference amounts to ~ 8 K in TIRVIM data and to 10K in MCS data at 40 Pa, corresponding to tide amplitudes of 4–5K (assuming that the diurnal tide extrema peaks near 3am at this pressure level). Previous investigations from MCS at the same season ($L_s=135$ – 165°) in MY28 reported a peak-to-peak 3pm–3am temperature difference between 5K and 10K at the equator and 30 Pa (a T_{diff} value between 2.5 and 5K, Lee et al., 2009), which is commensurate to our findings. We caution however that the 3pm–3am temperature difference cannot be completely trusted as an absolute measure of the peak-to-peak amplitude of the diurnal tide, as it is impossible to know the timing of the temperature extrema from these two local times alone. This is particularly true near 50°N at $L_s=150^\circ$: here, DW1 is found to have a maximum amplitude near 30 Pa, with temperature extrema occurring near 6h (and not 3h), so that taking the 3pm–3am temperature difference would underestimate the diurnal tide amplitude. This represents a relatively small error, but if the phase of the thermal tide is even more shifted or changes with seasons (significant interannual variations of the tide phases have indeed been reported by Steele et al. (2021)), the 3pm–3am temperature difference then becomes a poor metrics of the tide amplitudes.

621 Identifying the semi-diurnal tide from along-track MCS data alone is not possible,
622 as only two local times are available. More precise estimates of the tide amplitudes and
623 phases (for both the diurnal and semi-diurnal tides) can be derived by combining along-
624 track and cross-track MCS data, covering altogether six different local times per day. This
625 strategy has been exploited by Kleinböhl et al. (2013); Wu et al. (2015, 2021); Steele et
626 al. (2021). However, at low to mid-latitudes, the MCS local time coverage is limited to
627 ± 1.5 hours from 3am or 3pm, resulting in a large local time range without coverage over
628 which one has to interpolate. Small errors in the temperature profiles can lead to large
629 uncertainties when decomposing the tides' parameters. For instance, Kleinböhl et al. (2013)
630 estimated the semi-diurnal tide amplitude to be 6–8 K in the 1–10 Pa equatorial region
631 at $L_s=100^\circ$ of MY31, but with a 5K uncertainty. We also note that the vertical cover-
632 age of temperature profiles obtained from MCS observations (along and cross-track) can
633 be severely limited in the lower atmosphere due to aerosols, which is often the case at
634 equatorial latitudes where the semi-diurnal tide is expected to peak, limiting the deter-
635 mination of semi-diurnal tide parameters to pressures lower than ~ 30 Pa. At higher lat-
636 itudes (beyond 60°), the local time range covered by MCS increases based on the mea-
637 surement geometry, leading to a more robust determination of tide parameters. The same
638 authors derived a greater amplitude of the semi-diurnal tide at winter high latitudes (60°S);
639 unfortunately, our results are limited to mid-latitudes (40°S) and we cannot make such
640 a comparison here. Wu et al. (2015) extended this work to two full martian years. Their
641 derived tide amplitudes are in good agreement with ours at $L_s=150^\circ$ (for MY31): they
642 report a 4–5K amplitude for the diurnal tide near 30 Pa and an increasing amplitude with
643 height of the semi-diurnal mode, ranging from 2 ± 2 K to 5 ± 2 K going from 10 to 2 Pa
644 (note that this 2K uncertainty is likely underestimated due to uneven local time sam-
645 pling). Regarding the meridional structure of the phase of DW1, our results agree qual-
646 itatively with that of Wu et al. (2021), shown at $L_s=90^\circ$ and 180° for MY33, with mid-
647 latitudes ($30\text{--}60^\circ$) showing downward phase propagation similarly to what is seen in TIRVIM
648 data. However, no strong north/south asymmetry in the vertical wavelength is reported
649 by the authors, which might be a phenomenon specific to the season ($L_s=150^\circ$) and/or
650 martian year studied here.

651 These favorable comparisons show that the study of migrating thermal tides, which
652 have long vertical wavelengths, with a nadir-viewing sounder, lead to quantitatively ro-
653 bust results – at pressures greater than ~ 5 Pa – despite its rather coarse vertical reso-

654 lution. This is very complementary to what MCS data analysis can achieve. Our results
655 confirm previous findings that semi-diurnal tides are important even in seasons of low
656 to moderate dust amounts (Kleinböhl et al., 2013). The authors had shown that the ra-
657 diative effect of clouds was an important driver of the semi-diurnal mode, resulting in
658 strong amplitudes of SW2 at high altitudes (10–12K at 1 hPa) and a moderate 4K am-
659 plitude at the equator down to 50 Pa (consistent with our observations). The important
660 role of clouds on forcing SW2 was also highlighted by Wilson et al. (2014) and Haberle
661 et al. (2019) who showed a continuous effect in the aphelion season, even at $L_s=150^\circ$.
662 Our results thus seems to confirm this prediction. The height of the cloud deck will be
663 centered at a higher altitude at $L_s=150^\circ$ due to the warming of the atmosphere relative
664 to $L_s=100^\circ$. Interestingly, a re-analysis of the tide amplitudes from TIRVIM at $L_s=90^\circ$
665 (first shown in Fan, Guerlet, et al., 2022), with seasonal de-trending applied, reveal a
666 3K equatorial semi-diurnal tide amplitude for $p<10$ Pa. The stronger, 4–5K SW2 am-
667 plitude at $p<10$ Pa at $L_s=150^\circ$ might align with cloud radiative forcing being shifted at
668 higher altitudes.

669 We remind that the Mars PCM does include such radiative forcings by clouds. The
670 fact that the PCM reproduces qualitatively the observed semi-diurnal tide amplitude and
671 phase (in the range 30°S – 30°N where TIRVIM results are the most reliable) indicates that
672 these forcings are well taken into account, at least to first order.

673 4 Thermal structure and tides during the global dust event

674 With visible dust column optical depth greater than 2 over most of the martian
675 globe for more than 60 sols (Kass et al., 2020), the global dust event of Martian Year
676 34 significantly impacted the dynamics and thermal structure of its atmosphere. Below
677 we report on the diurnal average temperature derived from TIRVIM during the storm
678 as well as the corresponding migrating tide parameters.

679 4.1 Diurnal mean thermal structure

680 The diurnal mean temperature derived during the MY34 Global Dust Event ($L_s=204^\circ$
681 on average) is shown in Fig. 12. Compared to the situation described in section 3.1, daily
682 averaged temperatures have significantly increased (by +40–45K) in the range 50°S – 30°N ,
683 going from 180–185K at $L_s=150^\circ$, $p=100$ Pa to 220K at $L_s=204^\circ$. At lower pressures,

684 the temperature during the GDE is also very high (200K at 10 Pa instead of 155–160K
685 a few months earlier). Elevated temperatures at $p < 50$ Pa are indeed a well-known char-
686 acteristics of GDE (Kass et al., 2020). In addition, a branch of warm descending air is
687 seen at high northern latitudes, with temperatures reaching 205–210K on a daily aver-
688 age, located above a cold polar vortex in the lower atmosphere. We report a strong merid-
689 ional gradient at altitudes below the 30 Pa level, with temperatures decreasing for in-
690 stance from 220K (100 Pa, 20°N) to 165K (60°N). A more moderate equator-to-pole tem-
691 perature gradient exists towards high southern latitudes, with temperatures still of 200K
692 at 70°S throughout the lower atmosphere. Temperatures simulated with the Mars PCM
693 are in very good agreement with the observations except for a steeper meridional gra-
694 dient in the modeled lower atmosphere. This corresponds to a ~ 5 K too cold simulated
695 polar vortex in the lower atmosphere, beyond 50°N and for $p > 100$ Pa.

696 Interestingly, several authors report that in the afternoon, the lower atmosphere
697 (at 50 Pa) is warmer at mid-southern latitudes than at mid-northern ones during the GDE
698 (Kass et al., 2020; Vlasov et al., 2022), linked with enhanced radiative forcing of the dust
699 in the southern hemisphere (both due to the insolation at the current season, and the
700 fact that there is more dust in the southern hemisphere during the peak of the storm).
701 However, we see that on a diurnal mean basis, northern tropics are warmer than the south-
702 ern ones at 50 Pa. This is consistent with the fact that the diurnal mean temperature
703 also reflects warming from the circulation, namely the warm descending branch located
704 in the northern hemisphere. Unfortunately, due to the failing of the wave mode decom-
705 position at $p < 10$ Pa south of 50°S (probably due to incorrect seasonal de-trending and
706 hence, a subtle mix of seasonal and local time variations that is not fitted by our Eq. 1),
707 we cannot firmly conclude on the presence or not of a southern counterpart of this cir-
708 culation branch in TIRVIM observations. However, given the excellent comparison with
709 the model at other latitudes, we can reasonably rely on the behavior of the Mars PCM,
710 which does not exhibit such a warm branch at high southern latitudes. In the simula-
711 tion, the diurnal mean temperature is only moderately warmer at $p < 10$ Pa towards very
712 high southern latitudes (south of 85°S, not shown). The diurnal mean temperature thus
713 reflects primarily a solsticial-type circulation, with upwelling at high southern latitudes
714 and downwelling at mid- and high- northern latitudes. This is consistent with the cur-
715 rent season ($L_s = 210^\circ$) and the rapid transition between the two-cell equinoxial-type cir-
716 culation and the one-cell solsticial-type circulation.

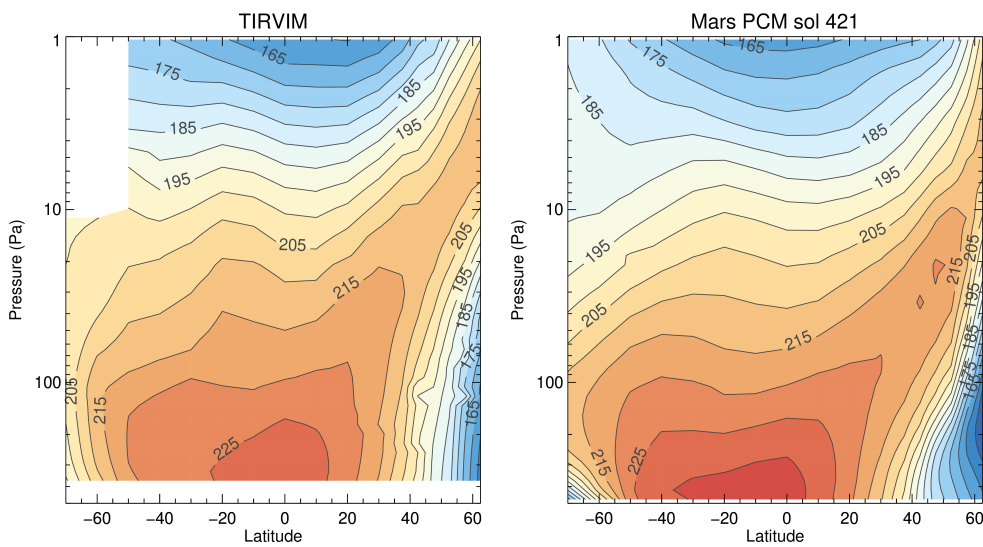


Figure 12. Latitude-pressure cross section of the diurnal mean temperature derived from ACS/TIRVIM (left) and as predicted from the Mars PCM (right) during the global dust event of MY34. We show here the Mars PCM output corresponding to sol 421 ($L_s=208^\circ$), ie. a few days later than the middle of our observation period, as there is a lag of a few sols in the simulated dust distribution compared to MCS observations (see for instance Fig. 12 in Young et al. (2022)). Choosing a slightly earlier or later date does not change our results.

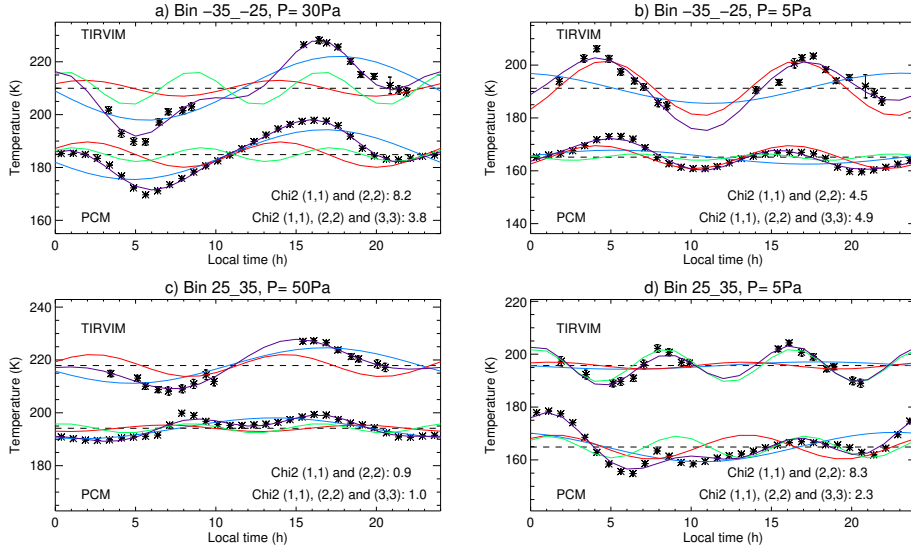


Figure 13. Examples of tide decomposition during the Global Dust Event for several latitude bins and pressure levels, as labeled. The zonally-averaged temperatures as measured by TIRVIM, as a function of local time, are shown as black stars. The fitted diurnal mean temperature is shown as a horizontal dashed line while the colored lines represent the fitted contributions from the diurnal (in blue), semi-diurnal (in red) and ter-diurnal (in green, when applicable) modes. The sum of these contributions (best fits to the data) is shown in purple. In addition to TIRVIM observations, we display the Mars PCM tide decomposition, shifted by -25K . Values of the χ^2 corresponding to TIRVIM observations are also given, with and without fitting the ter-diurnal mode.

717

4.2 Tide characteristics

718

719

720

721

On top of the $\sim 40\text{K}$ overall warming effect of the GDE at the diurnal mean scale at most latitudes (outside the cold polar vortex), very large tide amplitudes are observed during the storm. Before presenting the results, we briefly report on the detection of ter-diurnal tide signatures below.

722

4.2.1 Extraction of the ter-diurnal mode

723

724

725

726

Despite the rather limited local time coverage, we attempted to retrieve the amplitude and phase of the ter-diurnal mode (TW3) during the GDE, hence amounting to a total of 7 parameters to fit instead of 5 in the previous case. This is motivated by the expected amplitudes of up to $4\text{--}5\text{K}$ of this mode during dust storms, as noticed in the

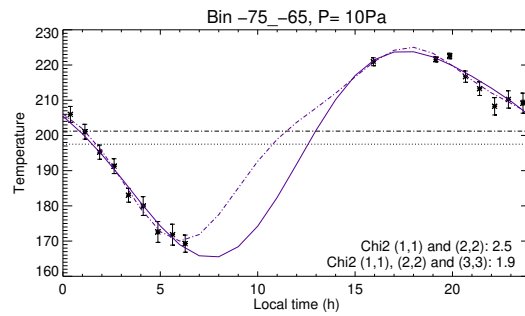


Figure 14. Zonally-averaged temperature as a function of local time as measured by TIRVIM (black stars) during the GDE, for the bin centered at 70°S and $p=10$ Pa. Best fits to the data are shown in purple with only the DW1 and SW2 modes (solid line) or including the TW3 mode (dot-dashed line). The fitted diurnal mean temperature is shown as horizontal dot-dashed or dotted lines whether the TW3 mode was included or not. This case illustrates the worst example of the degeneracy in fitting tide parameters, due to a large gap in local time coverage.

727 Mars PCM simulations. For some latitude bins and pressure levels, significantly better
 728 fits to the temperature data are indeed obtained with 7 instead of 5 parameters. Two
 729 of the best examples are shown in Fig. 13 for the bins centered at 30°N near 5 Pa, and
 730 30°S near 30 Pa (panels a and d). However, at high latitudes, the local time coverage
 731 is sometimes too sparse to confidently retrieve the tide parameters. For instance, fitting
 732 the ter-diurnal tide parameters for the bin centered at 70°S leads to a better χ^2 (com-
 733 pared to fitting 5 parameters) but the reconstructed temperatures obtained with or with-
 734 out fitting TW3 are largely inconsistent at missing local times (see Fig. 14). This fig-
 735 ure illustrates well the degeneracy among different solutions. A similar behavior is no-
 736 ticed for the bins centered at 60°S and 60°N (although less extreme). For this reason,
 737 we proceed by running the decomposition method for both 5 and 7 parameters and keep
 738 the solution with a significantly better χ^2 , except for the bins centered at 60°N, 60°S and
 739 70°S, where we choose to present results obtained with only 5 fitted parameters (DW1
 740 and SW2 only). TW3 is only confidently constrained between 60°S and 40°N and ~ 10
 741 and 50 Pa, with derived amplitudes of 4 to 6K. The fit to the high southern latitude data
 742 remains unsatisfactory for $p < 10$ Pa in any case, hence we will not interpret results in
 743 this region. Other examples of fits to the zonal mean temperature are shown in Fig. 15.

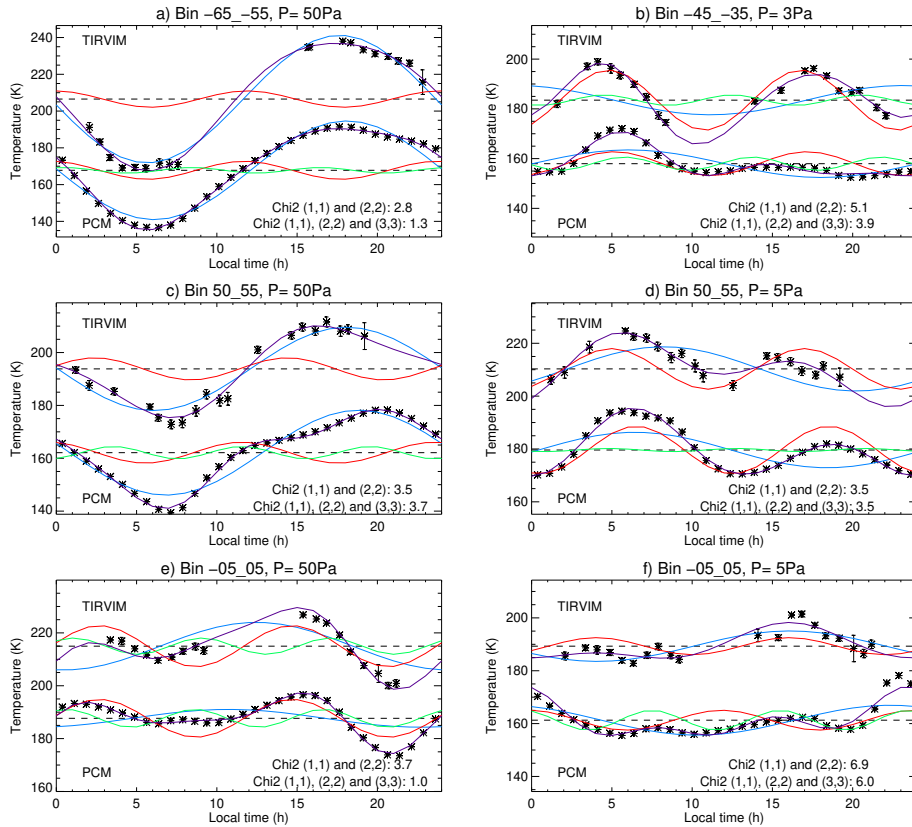


Figure 15. Same as Figure 13 for other latitude bins and pressure levels. Results from the Mars PCM were shifted by -25 K except for the bin 60° S, 50 Pa (shift of -50 K) and the bin 50 N, 50 Pa (shift of -40 K).

4.2.2 *Tide amplitudes*

We present the latitude-pressure cross-sections of the derived phase and amplitude for DW1, SW2 and TW3 in Fig. 16. The main striking feature in the tide structure is a huge diurnal tide amplitude at high southern latitudes, reaching 35K (hence, a peak-to-peak temperature variation of 70K) at 60°S and 50 Pa. This is six to seven times higher than the tide amplitude derived at extra-tropical latitudes at $L_s=150^\circ$, a few months earlier. This amplitude is even larger than the value of 29K reported by Kleinböhl et al. (2020) at 60°S from the 3am-3pm temperature difference in MCS observations, which can be explained by the fact that temperature extrema occur near 6am and 6pm (and not 3am and 3pm), as can be seen in the fits to the data in Fig. 15. Our derived amplitude is also significantly greater than the peak amplitude of 20–22K reported by Guzewich et al. (2014) from TES limb measurements obtained at 2am and 2pm during the 2001 GDE. In the northern hemisphere, another local maximum is present in DW1, reaching 17K at 45°N. This is close to the 15K amplitude reported near 50°N, 50 Pa by Kleinböhl et al. (2020) from MCS observations. Diurnal tide amplitudes are minimal and amount to 2–6K in a narrow region centered at 20°N in the lower atmosphere, and over a broader area (30°S–40°N) in the middle atmosphere, for $p < 50$ Pa. This pattern is very different from the pre-storm season, where the diurnal tide amplitude is known to be strong both near 50° latitude and the equator. This is consistent with the weakening of the diurnal tide at the equator during GDE as documented by Guzewich et al. (2014); Kleinböhl et al. (2013), although here we are able to better characterize the tide’s absolute amplitude and separate it from the contribution of the ter-diurnal tide.

The semi-diurnal tide also exhibits a very different pattern compared to the pre-storm season. Instead of being maximum at the equator, we find three localized regions of high amplitude. We report a first local maximum in the lower atmosphere near 100 Pa, where SW2 reaches an amplitude of 12K at latitude 20–40°S, while its amplitude is negligible in the opposite hemisphere. The SW2 signature is thus highly asymmetric between the two hemispheres at this pressure level. Secondly, for $p < 10$ Pa, we report two local maxima : one near 30–50°S (reaching 12K, hence twice as strong as the diurnal tide amplitude at this latitude and pressure level) and another one near 40–60°N (reaching 8K, commensurate to the diurnal tide there). Despite the lower sensitivity of TIRVIM at these lower pressure levels, the signature of the semi-diurnal tide is very clear in the data (see fits for the case 30°S, 5 Pa in Figure 13b and for 50°N, 5 Pa in Figure 15d). In this pres-

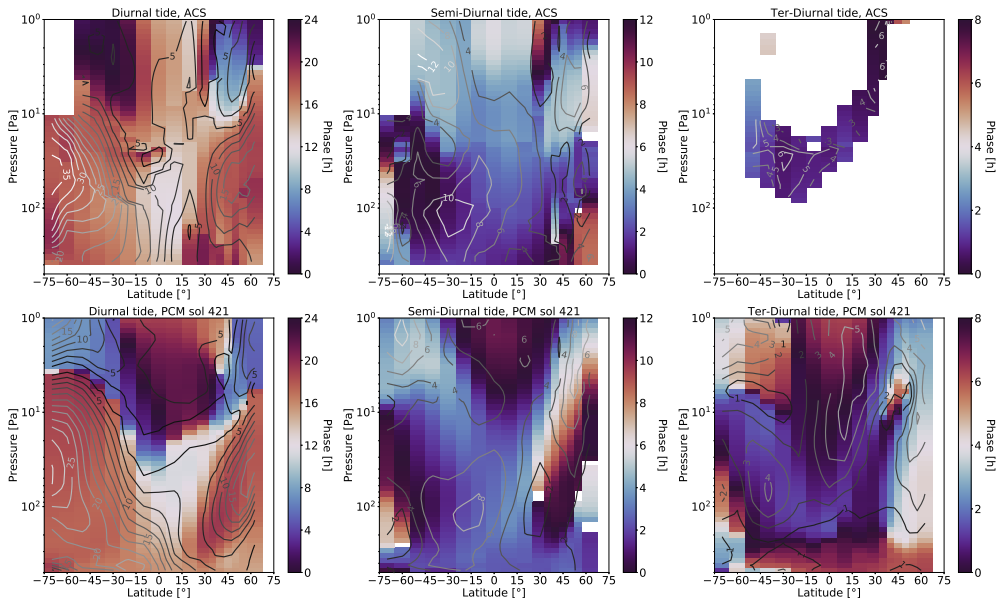


Figure 16. Phase (color, in hours) and amplitude (contours, in Kelvin) of the diurnal (left), semi-diurnal (middle) and ter-diurnal (right) migrating tide derived from ACS/TIRVIM (upper row) or from the Mars PCM (bottom row) during the global dust event of MY34, at sol 421 ($L_s=208^\circ$). Gaps in the ter-diurnal mode amplitude correspond to cases where the fit to the data was not improved when TW3 was included.

777 sure range ($p < 10$ Pa) the structure of the SW2 component is more symmetric with re-
778 spect to the equator. Modeling studies have suggested that during a GDE, the semi-diurnal
779 tide amplitude would rise significantly as a result of a larger quantity of dust over a broad
780 altitude range (Wilson & Richardson, 2000; Forbes & Miyahara, 2006). Data assimila-
781 tion of TES nadir observations during the MY25 global storm (Wilson et al., 2007) yielded
782 an amplitude of ~ 6 K for the equatorial SW2 component (expressed as a temperature
783 measured at $15\mu\text{m}$, representative of the 50 Pa level), which is commensurate to our de-
784 rived SW2 amplitude. According to this data assimilation, SW2 featured another local
785 maximum (6K as well) near 60°S during the MY25 global dust storm, while here we re-
786 port a local maximum near 30°S . This difference might be caused by different dust dis-
787 tributions among the storms.

788 The ter-diurnal tide amplitude is more difficult to assess given its lower amplitude
789 (on top of higher amplitude signals from the other two modes) and the limited local time
790 coverage. However, we can clearly assess its detection and relatively high amplitudes,
791 reaching 5–6K, in two distinct regions. The first maximum extends from 10 to 60°S and
792 15 to 50 Pa (roughly an altitude range in between the two SW2 local maxima at 30 – 40°S);
793 the second one is found near 20 – 40°N for $p < 10$ Pa (slightly to the south of a SW2 lo-
794 cal maxima). Including the ter-diurnal mode in these cases lead to a significant χ^2 re-
795 duction, by a factor of 2 to 3 (see Fig. 15). Interestingly, these maxima are located where
796 the SW2 amplitude is found minimum. Amplitude of TW3 of typically 0.5K were reported
797 during the aphelion season by Fan, Forget, et al. (2022) but to our knowledge, there is
798 no previous observational study of TW3 during dust storms.

799 We estimate the error on tide amplitudes to be of the order of 2K, reaching 3–4K
800 at high latitudes, based on measurement error, on incomplete diurnal coverage and on
801 imperfect "seasonal" de-trending. Similarly to the $L_s = 150^\circ$ case, the tide amplitudes are
802 expected to vary over the course of the 25-sols period considered here, as the storm is
803 evolving. For instance, in the Mars PCM, changes in amplitude of typically 2K are ev-
804 ident between sol 412 and sol 422 ($L_s = 204 - 209^\circ$). We can assume that this variabil-
805 ity is representative of reality and hence impacts our sensitivity.

806 Comparisons to tide characteristics extracted from the Mars PCM simulations are
807 shown in the bottom row of Fig. 16 as well as in the fits examples (Fig. 13 and 15). Note
808 here that we did not attempt to extract the model temperature profiles at TIRVIM ex-

809 act latitude, longitude, local time and date, due to the sparser local time coverage and
810 to avoid the potential effects of imperfect representation of the evolution of the dust storm
811 over the 25-sols period in the model. Rather, we present tide parameters extracted for
812 one representative martian sol number 421 ($L_s = 208^\circ$).

813 Overall, we find that the model reproduces very well the structure of DW1 dur-
814 ing the GDE: the location and amplitude of the two extrema qualitatively match the ob-
815 servations, although we report a tide amplitude 8K greater at high southern latitudes
816 compared to the Mars PCM (even without applying a vertical smoothing). The fact that
817 the tide minimum amplitude is located near 20°N (and not at the equator) in the lower
818 troposphere is also well reproduced. The amplitude of DW1 is found minimum (only 2K)
819 near 30 Pa at the equator, which is consistent with the weakening of the gravest Hough
820 mode of the diurnal tide due to increased dust loading in the simulations by Wilson and
821 Richardson (2000). The structure of SW2 in the Mars PCM also features striking sim-
822 ilarities to our observations, in particular with the display of a strong north-south asym-
823 metry in the lower atmosphere. Indeed, the SW2 amplitude reaches 8K in the model at
824 20°S and 100 Pa while it is minimum (less than 1K) at $20\text{--}30^\circ\text{N}$. The main difference is
825 that the latitude of these extrema are located $\sim 10^\circ$ closer to the equator than in the ob-
826 servations. In the upper part of the atmosphere, SW2 is found maximum near 50°N and
827 50°S in the Mars PCM, which qualitatively matches our findings, although in the obser-
828 vations, the southern maximum is more extended in pressure and latitude : its ampli-
829 tude is greater than 5K in the region $25\text{--}50^\circ\text{S}$ and $p < 10$ Pa, while it is restricted to 40--
830 50°S and $p < 3$ Pa in the model.

831 We also report an overall model-observation agreement for TW3. Indeed, ter-diurnal
832 tide amplitudes simulated with the Mars PCM feature a 4K local maximum near 40°S
833 and 50 Pa that matches the location of a corresponding extremum in TIRVIM observa-
834 tions. The simulated amplitudes are the strongest between 0° and 20°N for pressures less
835 than 30 Pa, where they reach 4–5 K. There is apparently no such broad low-latitude max-
836 imum in the observations, but a similarly high TW3 amplitude region is found around
837 30°N at pressures below 10 Pa in the observations, which could correspond to the struc-
838 ture seen in the model, but shifted towards the northern tropics for unknown reasons.

4.2.3 Tide phases and vertical structure

The phase structure of DW1 is found to differ completely from the pre-storm season. For $p > 10$ Pa, DW1 is now indeed dominated by the extra-tropical vertically-trapped Hough modes that are excited by strong dust radiative forcing, and that had a small influence at $L_s = 150^\circ$. In this pressure range, the phase of DW1 is locked at 5–6 pm through a large part of the extra-tropical atmosphere: up to 5–10 Pa at 30–60°S and up to 10–20 Pa at 30–60°N. This slight hemispheric asymmetry in the altitude range where DW1 is vertically-trapped is consistent with the expectation that the extratropical tide responds to local heating by dust, which extends higher in the southern hemisphere during the MY34 storm (Kleinböhl et al., 2020). A similar phase behavior was reported by Wu et al. (2021) from MCS data during the MY33 dusty season, and is also well reproduced by the Mars PCM or other previous modelling studies (Wilson & Richardson, 2000; Banfield et al., 2003). The vertically-propagating equatorial (1,1) Hough mode is clearly attenuated; rather, the equatorial region is strongly influenced by the extra-tropical modes. To further illustrate the meridional structure of the tide’s phases, we show in Fig. 17 the diurnal evolution of the reconstructed temperature field with latitude at a pressure of 50 Pa, from TIRVIM data and from the Mars PCM, along with the reconstructed signals from the diurnal and semi-diurnal tides. Left panels of this figure compares quite well with the ones presented in Wilson and Richardson (1999), showing the diurnal evolution of the T_{15} temperature simulated and measured by the Viking mission during the 1977 storms. A similar figure for the $L_s = 150^\circ$ case is presented in Fig. 17. Note that the 6 pm phase of DW1 at high latitudes is similar at $L_s = 150$ or during the GDE: the storm does not impact the timing of the extrema but reinforces their amplitude. Rather, at the equator, the DW1 phase during the GDE (eg., noon at 50 Pa) is intermediate between the pre-storm one (6 am at 50 Pa at $L_s = 150^\circ$) and the high-latitude one. A similar phase structure is predicted by the Mars PCM for $p > 10$ Pa.

At lower pressures, we report abrupt phase changes at mid-latitudes during the GDE, but with opposite behavior in the two hemispheres. At 40–60°N, the phase rapidly shifts from 6 pm for $p > 10$ Pa towards earlier local times of 6–8 am for $p < 10$ Pa. On the other hand at 20–60°S, the phase changes more gradually from 5–6 pm ($p > 10$ Pa) to later local times, reaching midnight at $p = 2$ Pa, i.e. corresponding to an upward-propagating phase (see Fig. 19). Abrupt phase shifts are also predicted by the Mars PCM at mid-latitudes and follow quite well the observed ones up to $p = 5$ Pa. At even lower pressures,

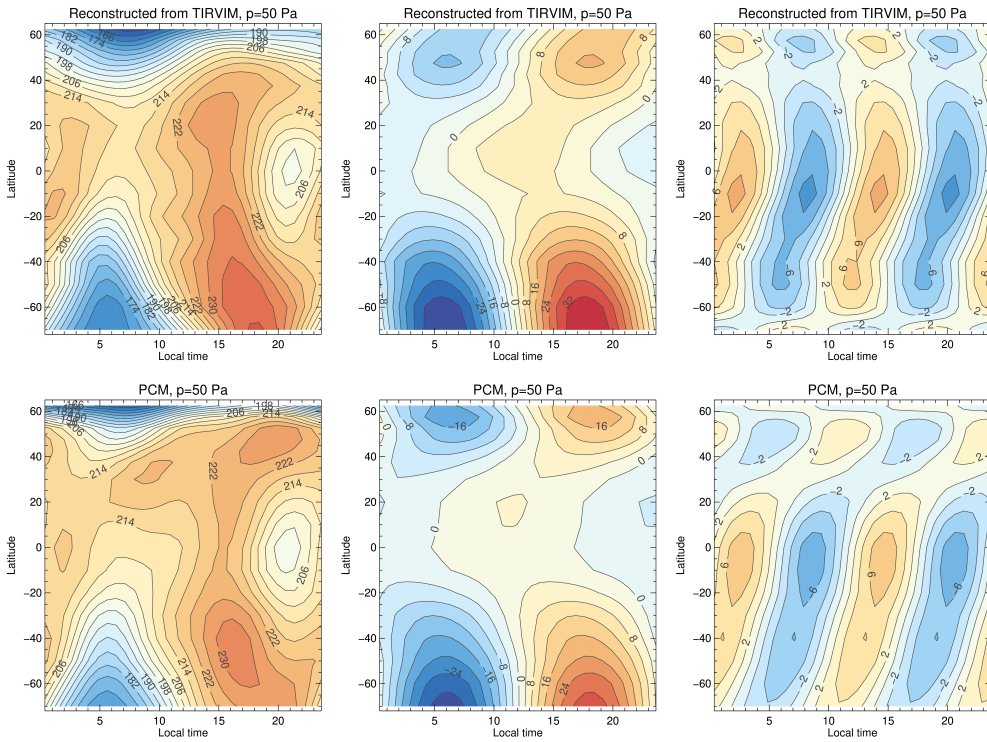


Figure 17. Left: Diurnal variation of the temperature at $p=50$ Pa reconstructed from fitting TIRVIM data (top) or from the Mars PCM (bottom) during the global dust event of MY34. The middle and right panels show the reconstructed diurnal and semi-diurnal modes, respectively.

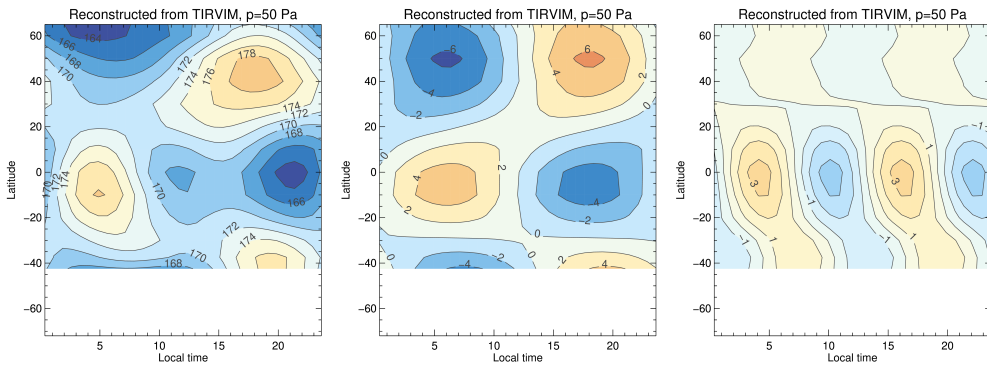


Figure 18. Same as Fig. 17, but reconstructed from TIRVIM observations at $L_s=150^\circ$.

872 the phase at 40°S suddenly changes to 6 am in the Mars PCM, which does not match
873 the observations, while the phase at mid-northern latitudes starts to increase towards
874 later local times (see Fig. 19). Retrieving correctly abrupt phase changes from nadir ob-
875 servations is challenging in this pressure range, as TIRVIM information content quickly
876 decreases for $p < 10$ Pa and has a broader contribution function, leading to an underes-
877 timation of the tide's amplitudes. The smaller the tide amplitude, the more difficult it
878 is to assess its phase, especially given the uneven local time sampling. However, some
879 model-observation mismatches appear quite robust when looking at the fits to the data.
880 For instance at 40°S and 3 Pa, the amplitude of SW2 is almost three times greater in
881 the observations than in the PCM, with temperature maxima at 4am and 4pm of sim-
882 ilar amplitude (see panel b of Fig. 15). If the phase of DW1 was indeed at 6am (as pre-
883 dicted by the PCM), the 4pm temperature maximum corresponding to SW2 would be
884 compensated by the temperature minimum of DW1 at 6pm, which is not the case. In
885 addition, we recall that our a priori temperature profile does not contain information on
886 the phase (it is the same at all local times) so that our retrievals are not biased in that
887 respect. Hence, the phase signatures reported at $p < 10$ Pa look rather robust.

888 The different phase characteristics between the northern and southern hemispheres
889 might be related to the different vertical distribution of water ice clouds at 40–60°S and
890 40–60°N. Indeed, Wu et al. (2021) also found examples of upward phase propagation of
891 the diurnal tide from 10 to 1 Pa in the southern hemisphere during major regional dust
892 storms. The authors linked this behavior to the thermo-tidal forcing by high altitude (~ 1 Pa)
893 water ice clouds. Our results at least partly support this theory, as elevated water ice
894 clouds were also reported during the MY34 GDE (Stcherbinine et al., 2020). The ele-
895 vated SW2 amplitude that we derive from TIRVIM at high altitudes also supports a sig-
896 nificant forcing by water ice clouds, which could be underestimated in the Mars PCM
897 due to unrealistic water ice properties (particle sizes for instance) and/or spatial distri-
898 bution. However, elevated clouds were apparently present in similar amounts in the south-
899 ern and northern hemisphere during the MY34 GDE (Liuzzi et al., 2020), so that this
900 does not fully explain why only mid-southern latitudes exhibit an upward-propagating
901 phase behavior. The quantitative impact of these forcings on the tides' phase structure
902 remains to be further investigated in future studies. Note that data assimilation of TIRVIM
903 temperature and dust retrievals in the Mars PCM does not produce an upward-propagating
904 phase at southern mid-latitudes (see Fig. 19 in Young et al., 2022): this might be be-

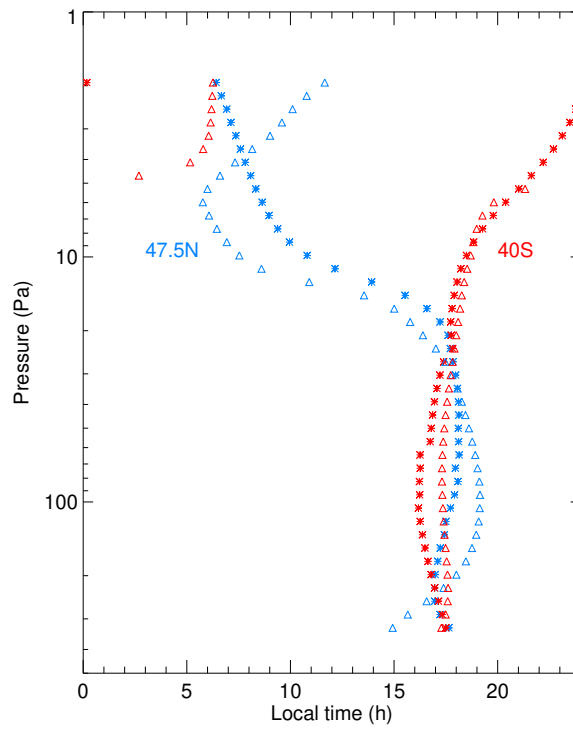


Figure 19. Phase of the diurnal tide with pressure at 40°S (red) and 47.5°N (blue) during the MY34 GDE ($L_s \sim 200^\circ$) as derived from ACS/TIRVIM (stars) and as predicted by the Mars PCM (triangles).

905 cause about half of TIRVIM vertical profiles were not included in the assimilation for
906 $p < 5$ Pa (due to their lower information content). An assimilation including water ice cloud
907 observations would also further improve the analysis. Finally, we also report a different
908 phase structure for DWI between the observations and the model in the equatorial re-
909 gion for $p < 30$ Pa: in the observations, the phase does not vary much with altitude (it
910 stays in the range noon-3pm throughout the atmosphere) while the phase varies a lot
911 and reaches 9pm at $p = 5$ Pa in the Mars PCM. Data assimilation of TIRVIM observa-
912 tions does yield a significant phase change in the analysis compared to the PCM sim-
913 ulations (Young et al., 2022), but the physical reasons behind this observation-model mis-
914 match in phase remains unknown.

915 Regarding the semi-diurnal tide, we find that the temperature peaks at ~ 3 am near
916 the equator (4AM before the storm) in the lower atmosphere. This is in excellent agree-
917 ment with the tidal model experiments made by Wilson and Richardson (2000), in the
918 case of a high atmospheric dust content, and with the observations by the Viking Infrared
919 Thermal Mapper during the 1977b storm discussed by the authors. The SW2 phase ver-
920 tical and meridional structure reported from TIRVIM is similar to the one predicted by
921 the Mars PCM except in two regions: 1) at low latitudes and $p < 10$ Pa, where we derive
922 a phase of 6am instead of noon in the Mars PCM; and 2) at northern mid-latitudes be-
923 tween 10 and 100 Pa, where there is also a 6h out-of-phase difference between TIRVIM
924 and the PCM. Note that these observation-model mismatches occur where the ampli-
925 tude of SW2 is rather low (2-4K), making the phase determination challenging from the
926 observations. However, looking at the data directly (see Fig. 13), it is clear that the di-
927 urnal evolution of the temperature at 30°N , 50 Pa is not well captured by the Mars PCM:
928 instead of featuring a local minimum near 8 AM, the model predicts a local tempera-
929 ture maximum at this time of the day. Another striking disagreement is displayed for
930 the bin 30°N at 5 Pa, where diurnal variations in TIRVIM are clearly dominated by the
931 ter-diurnal tide while in the Mars PCM, DW1, SW2 and TW3 contribute almost equally.
932 It is also worth noting that the model-observation mismatches in phase and amplitude
933 north of 30°N occur where the latitudinal temperature gradient also disagree at the di-
934 urnal mean scale. According to Wu et al. (2017), differences in meridional gradient, hence
935 of vertical shear of the zonal wind, could impact the vertical propagation of waves, hence
936 the tides's phases. Other potential sources of observation-model mismatch are an incor-

937 rect vertical distribution of aerosol (dust and water ice clouds), or incorrect represen-
938 tation of wave forcings such as gravity waves.

939 Fig. 17 highlights that the SW2 phase drifts slowly earlier in the day at higher lat-
940 itudes, with peaks occurring near noon and midnight at 60°S and 60°N. This behavior
941 was not present before the storm (see Fig. 18). A similar phase tilt is seen in the Mars
942 PCM at 50 Pa in the southern hemisphere. Such a shift implies that asymmetric Hough
943 modes contribute significantly to the semi-diurnal tide pattern. Indeed, if the gravest Hough
944 function (equatorially symmetric) was the only contributor, there would be no phase shift
945 with latitude. Interestingly, such a phase tilt was reported among the surface pressure
946 measurements made by the Viking landers at 22°N and 48°N during the 1977 storms and
947 has been successfully explained assuming asymmetric thermotidal forcing between the
948 two hemispheres, namely an asymmetric dust distribution (Bridger & Murphy, 1998).
949 As there was indeed more dust in the southern hemisphere during the MY34 GDE, this
950 characteristics is certainly the reason behind the hemispheric asymmetry of the SW2 mode
951 and its phase tilt with latitude.

952 5 Conclusion

953 In this paper, we reported on the migrating tide amplitudes and phases derived from
954 the analysis of vertical temperature profiles, themselves retrieved from the TIRVIM-ACS
955 instrument onboard the ExoMars Trace Gas orbiter in April–July 2018, before and dur-
956 ing the MY34 Global Dust Event. The strength of the TIRVIM observations is to cover
957 a great variety of local times, although a complete coverage of diurnal cycle takes 54 sols,
958 mixing to a certain extent seasonal with diurnal variations. To make the most out of TIRVIM
959 observations, we used contemporaneous temperature profiles from the MCS limb sounder
960 to seasonally de-trend TIRVIM temperatures. We have shown that this improved the
961 derived semi-diurnal tide amplitudes and phases. We summarize below the main find-
962 ings on tide characteristics at the two considered seasons.

963 At $L_s=150^\circ$, the latitude/pressure structure of the migrating tides captured by TIRVIM
964 are in excellent agreement with that predicted from tidal theory: their latitudinal struc-
965 tures correspond to the theoretical ones. DW1 is dominated by the gravest (1,1) Hough
966 function, with vertically-propagating tides at the equator, a minimum amplitude near
967 30°, and again a downward phase propagation near 50° latitude corresponding to the neg-

968 active lobes of the (1,1) Hough function: the vertically-trapped modes that are expected
969 to dominate at high latitudes does not seem to influence the mid-latitudes at this sea-
970 son. The derived amplitudes, of typically 4–5K at the equator for the diurnal mode, and
971 2–4K for the semi-diurnal mode, are very similar to that obtained from the Mars PCM
972 once TIRVIM averaging kernels are applied to the modeled profiles. The main features
973 of the migrating tides are well reproduced in the PCM, including the slight off-equatorial
974 maximum amplitudes observed at 5–10°S at this season. Vertical wavelengths at the equa-
975 tor are similar in both the model and the observations, with values of 4.4 scale heights
976 (H) for the diurnal tide and 7.3 H for the semi-diurnal tide at the equator. This suggests
977 that the thermotidal forcing in our general circulation model and the atmospheric re-
978 sponse to it is realistic. The only significant disagreement found is a small (1 hour and
979 a half) phase shift of the diurnal mode, with temperature extrema occurring too late in
980 the model. This was already reported by Fan, Guerlet, et al. (2022) and Fan, Forget, et
981 al. (2022) and remains to be explained. Differences in the vertical, meridional or zonal
982 distribution of aerosols between model and observations could play a role in this phase
983 shift, as well as as interferences with non-migrating tides (eastward-propagating Kelvin
984 modes).

985 During the MY34 GDE, we report strong amplitudes of the diurnal tide near 60°S
986 and 50°N, being maximum near 50 Pa and amounting to 35K and 17K, respectively, and
987 being vertically-trapped up to 20–5 Pa. Thanks to TIRVIM we can more clearly assess
988 the phase of tides during the GDE, with a temperature maximum occurring near 6 PM
989 for the mid and high latitude observations up to ~ 20 Pa, which is similar to that before
990 the storm at these high latitudes and this pressure level. On the other hand, the ampli-
991 tude of the diurnal mode at the equator has remain similar (for $p > 50$ Pa) or smaller (for
992 $p < 50$ Pa) compared to that before the storm, in agreement with the predictions that the
993 gravest (1,1) Hough function is weakened by significant dust loading (Wilson & Richard-
994 son, 2000). The amplitude of the SW2 mode is increased during the storm, reaching 8–
995 12K at $p = 1–10$ Pa and $p = 70–300$ Pa. However, these high amplitudes are well offset from
996 the equator and are located near 20–30°S. We assess for the first time in the tempera-
997 ture field the phase of the SW2 mode during a GDE, which corresponds to maxima near
998 3 AM and 3 PM near the equator, with a phase tilt with latitude (earlier maxima at high
999 latitudes). This characteristics is consistent with the tidal model experiments of Bridger
1000 and Murphy (1998), in which a hemispheric asymmetry in dust distribution increases

1001 the importance of the asymmetric Hough functions and results in a meridional phase tilt
1002 in the surface pressure signature of SW2. We also report hints of upward-propagating
1003 phase of the diurnal tide at mid-southern latitudes for $p < 10$ Pa, which remains to be fur-
1004 ther investigated and might be linked to a thermo-tidal forcing by elevated water ice clouds
1005 (Wu et al., 2021). Finally, we detected for the first time signals of the ter-diurnal tide
1006 during the storm, amounting to 6K near 30°S, 20–50 Pa and near 30°N, 1–10 Pa. Most
1007 of these characteristics are qualitatively consistent with the Mars PCM run with the dust
1008 scenario for MY34 (i.e. with dust column values imposed to match that observed from
1009 the Mars Climate Sounder during that year, with a simple linear interpolation between
1010 two successive sols to represent diurnal variations). Minor model-observations disagree-
1011 ments are noticed regarding the tides characteristics and the diurnal mean thermal struc-
1012 ture that reflect slight differences in the strength of the Hadley circulation and in the
1013 location of the edge of the polar vortex, hence on the conditions for vertical propagation
1014 of the waves. The vertical distribution of dust and water ice clouds, and its diurnal vari-
1015 ation, are also known to be imperfect in the Mars PCM, which could also explain the
1016 model-observation mismatches. However, these disagreements remain small, implying
1017 that with correct thermo-tidal forcing (to first order), our model reproduces well the re-
1018 sponse of the atmosphere to high dust contents. It will be interesting to investigate in
1019 the future the characteristics of the non-migrating tides during the GDE. This might be
1020 challenging from TIRVIM observations due to their rather limited local time coverage
1021 (two times six hours in the period considered in this paper), but other instruments with
1022 denser local time coverage such as EMIRS onboard EMM might witness another GDE
1023 and shed more light on these phenomena. Data assimilation of several datasets (tem-
1024 perature, dust, water ice; from nadir and limb sounders) should also be developed to bet-
1025 ter constrain the tide’s characteristics without being hampered by the mix of secular trends
1026 and diurnal variations inherent to TIRVIM observational scheme.

1027 6 Open Research

1028 Mars Climate Sounder data are publicly available on the Atmospheres Node of NASA’s
1029 Planetary Data System (McCleese, 2008). The TIRVIM temperature retrievals used in
1030 this paper are available in NetCDF format on the Institut Pierre Simon Laplace (IPSL)
1031 data server (Guerlet, 2021).

1032 Acknowledgments

1033 ExoMars is a space mission of ESA and Roscosmos. The ACS experiment is led by IKI,
 1034 the Space Research Institute in Moscow, assisted by LATMOS in France. This work, ex-
 1035 ploiting ACS/TIRVIM data, acknowledges funding by CNES. The science operations of
 1036 ACS are funded by Roscosmos and ESA. ACS/TIRVIM team at IKI acknowledges the
 1037 subsidy of the Ministry of Science and High Education of Russia. Simulations with the
 1038 Mars PCM used in this article were performed using HPC computing resources from GENCI-
 1039 CINES (Grant 2022-A0120110391). Armin Kleinböhl acknowledges support from NASA's
 1040 Mars Data Analysis program (80NM0018F0719). Work at the Jet Propulsion Labora-
 1041 tory, California Institute of Technology, is performed under contract with the National
 1042 Aeronautics and Space Administration. We thank John Wilson and an anonymous ref-
 1043 eree for their constructive comments that helped improve the contents of this manuscript.

1044 References

- 1045 Banfield, D., Conrath, B., Pearl, J. C., Smith, M. D., & Christensen, P. (2000,
 1046 April). Thermal tides and stationary waves on Mars as revealed by Mars
 1047 Global Surveyor thermal emission spectrometer. *jgr*, *105*(E4), 9521-9538. doi:
 1048 10.1029/1999JE001161
- 1049 Banfield, D., Conrath, B. J., Smith, M. D., Christensen, P. R., & Wilson, R. J.
 1050 (2003, February). Forced waves in the martian atmosphere from MGS TES
 1051 nadir data. *Icarus*, *161*(2), 319-345. doi: 10.1016/S0019-1035(02)00044-1
- 1052 Bridger, A. F. C., & Murphy, J. R. (1998, April). Mars' surface pressure tides and
 1053 their behavior during global dust storms. *Journal of Geophysical Research*,
 1054 *103*(E4), 8587-8602. doi: 10.1029/98JE00242
- 1055 Fan, S., Forget, F., Smith, M. D., Guerlet, S., Badri, K. M., Atwood, S. A., ...
 1056 Millour, E. (2022, September). Migrating Thermal Tides in the Martian At-
 1057 mosphere During Aphelion Season Observed by EMM/EMIRS. *Geophysical*
 1058 *Research Letters*, *49*(18), e99494. doi: 10.1029/2022GL099494
- 1059 Fan, S., Guerlet, S., Forget, F., Bierjon, A., Millour, E., Ignatiev, N., ... Korablev,
 1060 O. (2022, April). Thermal Tides in the Martian Atmosphere Near Northern
 1061 Summer Solstice Observed by ACS/TIRVIM Onboard TGO. *Geophysical*
 1062 *Research Letters*, *49*(7), e97130. doi: 10.1029/2021GL097130
- 1063 Forbes, J. M. (1995, January). Tidal and Planetary Waves. *Geophysical Monograph*

- 1064 *Series*, 87, 67. doi: 10.1029/GM087p0067
- 1065 Forbes, J. M., & Miyahara, S. (2006, July). Solar Semidiurnal Tide in the Dusty At-
1066 mosphere of Mars. *Journal of Atmospheric Sciences*, 63(7), 1798-1817. doi: 10
1067 .1175/JAS3718.1
- 1068 Forbes, J. M., Zhang, X., Forget, F., Millour, E., & Kleinböhl, A. (2020, Septem-
1069 ber). Solar Tides in the Middle and Upper Atmosphere of Mars. *Journal*
1070 *of Geophysical Research (Space Physics)*, 125(9), e28140. doi: 10.1029/
1071 2020JA028140
- 1072 Forget, F., Hourdin, F., Fournier, R., Hourdin, C., Talagrand, O., Collins, M., ...
1073 Huot, J.-P. (1999, October). Improved general circulation models of the Mar-
1074 tian atmosphere from the surface to above 80 km. *Journal of Geophysical*
1075 *Research*, 104(E10), 24155-24176. doi: 10.1029/1999JE001025
- 1076 Guerlet, S. (2021). *Acs/tirvim temperature and aerosol retrievals* [dataset]. ES-
1077 PRI/IPSL. Retrieved from [https://doi.org/10.14768/AB765EBA-0C1D-](https://doi.org/10.14768/AB765EBA-0C1D-47B6-97D6-6390C63F0197)
1078 [47B6-97D6-6390C63F0197](https://doi.org/10.14768/AB765EBA-0C1D-47B6-97D6-6390C63F0197) doi: 10.14768/AB765EBA-0C1D-47B6-97D6
1079 [-6390C63F0197](https://doi.org/10.14768/AB765EBA-0C1D-47B6-97D6-6390C63F0197)
- 1080 Guerlet, S., Ignatiev, N., Forget, F., Fouchet, T., Vlasov, P., Bergeron, G., ... Ko-
1081 rablev, O. (2022, February). Thermal Structure and Aerosols in Mars' Atmo-
1082 sphere From TIRVIM/ACS Onboard the ExoMars Trace Gas Orbiter: Validat-
1083 ion of the Retrieval Algorithm. *Journal of Geophysical Research (Planets)*,
1084 127(2), e07062. doi: 10.1029/2021JE007062
- 1085 Guzewich, S. D., Talaat, E. R., & Waugh, D. W. (2012, March). Observa-
1086 tions of planetary waves and nonmigrating tides by the Mars Climate
1087 Sounder. *Journal of Geophysical Research (Planets)*, 117(E3), E03010. doi:
1088 10.1029/2011JE003924
- 1089 Guzewich, S. D., Wilson, R. J., McConnochie, T. H., Toigo, A. D., Banfield, D. J., &
1090 Smith, M. D. (2014, March). Thermal tides during the 2001 Martian global-
1091 scale dust storm. *Journal of Geophysical Research (Planets)*, 119(3), 506-519.
1092 doi: 10.1002/2013JE004502
- 1093 Haberle, R. M., Kahre, M. A., Hollingsworth, J. L., Montmessin, F., Wilson, R. J.,
1094 Urata, R. A., ... Schaeffer, J. R. (2019, November). Documentation of the
1095 NASA/Ames Legacy Mars Global Climate Model: Simulations of the present
1096 seasonal water cycle. *Icarus*, 333, 130-164. doi: 10.1016/j.icarus.2019.03.026

- 1097 Kass, D. M., Schofield, J. T., Kleinböhl, A., McCleese, D. J., Heavens, N. G.,
 1098 Shirley, J. H., & Steele, L. J. (2020, December). Mars Climate Sounder
 1099 Observation of Mars' 2018 Global Dust Storm. *Geophys. Res. Lett.*, *47*(23),
 1100 e83931. doi: 10.1029/2019GL083931
- 1101 Kleinböhl, A., Schofield, J. T., Kass, D. M., Abdou, W. A., Backus, C. R., Sen, B.,
 1102 ... McCleese, D. J. (2009, October). Mars Climate Sounder limb profile re-
 1103 trieval of atmospheric temperature, pressure, and dust and water ice opacity.
 1104 *J. Geophys. Res.*, *114*(E10), E10006. doi: 10.1029/2009JE003358
- 1105 Kleinböhl, A., Spiga, A., Kass, D. M., Shirley, J. H., Millour, E., Montabone, L., &
 1106 Forget, F. (2020, January). Diurnal Variations of Dust During the 2018 Global
 1107 Dust Storm Observed by the Mars Climate Sounder. *Journal of Geophysical*
 1108 *Research (Planets)*, *125*(1), e06115. doi: 10.1029/2019JE006115
- 1109 Kleinböhl, A., Wilson, J. R., Kass, D., Schofield, J. T., & McCleese, D. J. (2013,
 1110 May). The semidiurnal tide in the middle atmosphere of Mars. *Geo-*
 1111 *phys. Res. Lett.*, *40*(10), 1952-1959. doi: 10.1002/grl.50497
- 1112 Korablev, O., Montmessin, F., Trokhimovskiy, A., Fedorova, A. A., Shakun, A. V.,
 1113 Grigoriev, A. V., ... Zorzano, M. P. (2018, February). The Atmospheric
 1114 Chemistry Suite (ACS) of Three Spectrometers for the ExoMars 2016 Trace
 1115 Gas Orbiter. *Space Sci. Rev.*, *214*(1), 7. doi: 10.1007/s11214-017-0437-6
- 1116 Lee, C., Lawson, W. G., Richardson, M. I., Heavens, N. G., Kleinböhl, A., Banfield,
 1117 D., ... Toigo, A. D. (2009, March). Thermal tides in the Martian middle
 1118 atmosphere as seen by the Mars Climate Sounder. *J. Geophys. Res.*, *114*(E3),
 1119 E03005. doi: 10.1029/2008JE003285
- 1120 Leovy, C. B., & Zurek, R. W. (1979, June). Thermal tides and Martian dust storms:
 1121 direct evidence for coupling. *Journal of Geophysical Research*, *84*, 2956-2968.
 1122 doi: 10.1029/JB084iB06p02956
- 1123 Lindzen, R. S. (1970, July). The Application and Applicability of Terrestrial At-
 1124 mospheric Tidal Theory to Venus and Mars. *Journal of Atmospheric Sciences*,
 1125 *27*(4), 536-549. doi: 10.1175/1520-0469(1970)027<0536:TAAAOT>2.0.CO;2
- 1126 Lindzen, R. S., & Chapman, S. (1969, October). Atmospheric Tides. *Space Science*
 1127 *Reviews*, *10*(1), 3-188. doi: 10.1007/BF00171584
- 1128 Liuzzi, G., Villanueva, G. L., Crismani, M. M. J., Smith, M. D., Mumma, M. J.,
 1129 Daerden, F., ... Patel, M. R. (2020, April). Strong Variability of Martian

- 1130 Water Ice Clouds During Dust Storms Revealed From ExoMars Trace Gas
 1131 Orbiter/NOMAD. *Journal of Geophysical Research (Planets)*, 125(4), e06250.
 1132 doi: 10.1029/2019JE006250
- 1133 Lo, D. Y., Yelle, R. V., Schneider, N. M., Jain, S. K., Stewart, A. I. F., England,
 1134 S. L., ... Jakosky, B. M. (2015, November). Nonmigrating tides in the Mar-
 1135 tian atmosphere as observed by MAVEN IUVS. *Geophysical Research Letters*,
 1136 42(21), 9057-9063. doi: 10.1002/2015GL066268
- 1137 Madeleine, J. B., Forget, F., Millour, E., Navarro, T., & Spiga, A. (2012, December).
 1138 The influence of radiatively active water ice clouds on the Martian climate.
 1139 *Geophysical Research Letters*, 39(23), L23202. doi: 10.1029/2012GL053564
- 1140 McCleese, D. J. (2008). *Mro mars climate sounder derived data records v1.0*.
 1141 [dataset]. NASA Planetary Data System. Retrieved from [https://doi.org/](https://doi.org/10.17189/P73K-XY37)
 1142 10.17189/P73K-XY37 doi: 10.17189/P73K-XY37
- 1143 McCleese, D. J., Schofield, J. T., Taylor, F. W., Calcutt, S. B., Foote, M. C., Kass,
 1144 D. M., ... Zurek, R. W. (2007, May). Mars Climate Sounder: An investigation
 1145 of thermal and water vapor structure, dust and condensate distributions in the
 1146 atmosphere, and energy balance of the polar regions. *Journal of Geophysical*
 1147 *Research (Planets)*, 112(E5), E05S06. doi: 10.1029/2006JE002790
- 1148 McLandress, C. (2002, March). The Seasonal Variation of the Propagating Diurnal
 1149 Tide in the Mesosphere and Lower Thermosphere. Part II: The Role of Tidal
 1150 Heating and Zonal Mean Winds. *Journal of Atmospheric Sciences*, 59(5),
 1151 907-922. doi: 10.1175/1520-0469(2002)059<0907:TSVOTP>2.0.CO;2
- 1152 Montabone, L., Spiga, A., Kass, D. M., Kleinböhl, A., Forget, F., & Millour, E.
 1153 (2020, August). Martian Year 34 Column Dust Climatology from Mars
 1154 Climate Sounder Observations: Reconstructed Maps and Model Simula-
 1155 tions. *Journal of Geophysical Research (Planets)*, 125(8), e06111. doi:
 1156 10.1029/2019JE006111
- 1157 Navarro, T., Madeleine, J. B., Forget, F., Spiga, A., Millour, E., Montmessin, F.,
 1158 & Määttänen, A. (2014, July). Global climate modeling of the Martian
 1159 water cycle with improved microphysics and radiatively active water ice
 1160 clouds. *Journal of Geophysical Research (Planets)*, 119(7), 1479-1495. doi:
 1161 10.1002/2013JE004550
- 1162 Stcherbinine, A., Vincendon, M., Montmessin, F., Wolff, M. J., Korablev, O., Fe-

- 1163 dorova, A., ... Shakun, A. (2020). Martian water ice clouds during the 2018
 1164 global dust storm as observed by the acs-mir channel onboard the trace gas
 1165 orbiter. *Journal of Geophysical Research: Planets*, 125(3), e2019JE006300.
 1166 Retrieved from [https://agupubs.onlinelibrary.wiley.com/doi/abs/](https://agupubs.onlinelibrary.wiley.com/doi/abs/10.1029/2019JE006300)
 1167 10.1029/2019JE006300 (e2019JE006300 10.1029/2019JE006300) doi:
 1168 <https://doi.org/10.1029/2019JE006300>
- 1169 Steele, L. J., Kleinböhl, A., Kass, D. M., & Zurek, R. W. (2021, April). Aerosols
 1170 and Tides in the Martian Tropics During Southern Hemisphere Spring Equinox
 1171 From Mars Climate Sounder Data. *Journal of Geophysical Research (Planets)*,
 1172 126(4), e06776. doi: 10.1029/2020JE006776
- 1173 Vlasov, P., Ignatiev, N., Guerlet, S., Grassi, D., Korablev, O., Grigoriev, D. n., ...
 1174 Montmessin, F. (2022, September). Martian Atmospheric Thermal Struc-
 1175 ture and Dust Distribution During the MY 34 Global Dust Storm From ACS
 1176 TIRVIM Nadir Observations. *Journal of Geophysical Research (Planets)*,
 1177 127(9), e07272. doi: 10.1029/2022JE007272
- 1178 Wilson, R. J., & Hamilton, K. (1996, May). Comprehensive model simulation of
 1179 thermal tides in the Martian atmosphere. *Journal of Atmospheric Sciences*,
 1180 53(9), 1290-1326. doi: 10.1175/1520-0469(1996)053
- 1181 Wilson, R. J., Lewis, S. R., & Montabone, L. (2007, July). Thermal Tides in an
 1182 Assimilation of Three Years of Thermal Emission Spectrometer Data from
 1183 Mars Global Surveyor. In LPI Editorial Board (Ed.), *Seventh international*
 1184 *conference on mars* (Vol. 1353, p. 3307).
- 1185 Wilson, R. J., Millour, E., Navarro, T., Forget, F., & Kahre, M. (2014, January).
 1186 GCM Simulations of aphelion season tropical cloud and temperature structure.
 1187 In F. Forget & M. Millour (Eds.), *Mars atmosphere: Modelling and observa-*
 1188 *tion, 5th international workshop* (p. 1304).
- 1189 Wilson, R. J., & Richardson, M. I. (1999, July). Comparison of Mars GCM Dust
 1190 Storm Simulations with Viking Mission Observations. In *The fifth interna-*
 1191 *tional conference on mars* (p. 6234).
- 1192 Wilson, R. J., & Richardson, M. I. (2000, June). The Martian atmosphere during
 1193 the Viking mission. I. Infrared measurements of atmospheric temperatures
 1194 revisited. *Icarus*, 145(2), 555-579. doi: 10.1006/icar.2000.6378
- 1195 Wu, Z., Li, T., & Dou, X. (2015, December). Seasonal variation of Martian middle

- 1196 atmosphere tides observed by the Mars Climate Sounder. *Journal of Geophys-*
1197 *ical Research (Planets)*, 120(12), 2206-2223. doi: 10.1002/2015JE004922
- 1198 Wu, Z., Li, T., & Dou, X. (2017, June). What causes seasonal variation of migrat-
1199 ing diurnal tide observed by the Mars Climate Sounder? *Journal of Geophys-*
1200 *ical Research (Planets)*, 122(6), 1227-1242. doi: 10.1002/2017JE005277
- 1201 Wu, Z., Li, T., Li, J., Zhang, X., Yang, C., & Cui, J. (2021, April). Abnormal Phase
1202 Structure of Thermal Tides During Major Dust Storms on Mars: Implica-
1203 tions for the Excitation Source of High altitude Water Ice Clouds. *Journal of*
1204 *Geophysical Research (Planets)*, 126(4), e06758. doi: 10.1029/2020JE006758
- 1205 Young, R. M. B., Millour, E., Guerlet, S., Forget, F., Ignatiev, N., Grigoriev, A. V.,
1206 ... Korablev, O. (2022, September). Assimilation of Temperatures and Col-
1207 umn Dust Opacities Measured by ExoMars TGO-ACS-TIRVIM During the
1208 MY34 Global Dust Storm. *Journal of Geophysical Research (Planets)*, 127(9),
1209 e07312. doi: 10.1029/2022JE007312
- 1210 Zurek, R. W. (1976, February). Diurnal tide in the Martian atmosphere. *Journal of*
1211 *Atmospheric Sciences*, 33, 321-337. doi: 10.1175/1520-0469(1976)033